

## ABSTRACT

WITTING, IAN THOMAS. Defect and Impurity Distributions in Traditionally Cast Multicrystalline and Cast Monocrystalline Silicon for Solar Substrates. (Under the direction of George Rozgonyi.)

An examination of two types of cast silicon was performed to correlate observed electrical properties with structural defects and chemical impurities. Results show that many of the significant impurities and defects occur as the result of controllable manufacturing methods. A unique sample of traditionally cast multicrystalline silicon (mc-Si) was obtained from BP Solar in April 2007. This sample was cut longitudinally and has intact the original edges of the ingot typically removed during processing. Impurity concentration profiles are compared directly with minority carrier lifetime maps to determine which impurities are most detrimental to the quality of the silicon. A minority carrier lifetime map was obtained using Microwave Photoconductance Decay (MW-PCD). Light element impurities (C, O) were profiled using Fourier Transform Infrared Spectroscopy (FT-IR) and metallic impurities were profiled by Deep Level Transient Spectroscopy (DLTS). Iron contamination was found to correlate best with reduction in minority carrier lifetime.

Silicon samples exposed to the environment of different furnaces used throughout the casting process were examined using Scanning Electron Microscopy (SEM) with Energy Dispersive Spectroscopy (EDS) and Secondary Ion Mass Spectroscopy (SIMS). This examination revealed the sources of many impurities observed in the final cast ingots. SEM and EDS were also used to examine impurity precipitation on samples taken from the tops of cast ingots. Carbide, nitride, and iron were found to be the primary contaminants that segregated to the ingot top.

A second unique sample of cast monocrystalline silicon, referred to as “mono-squared” and written as “Mono<sup>2</sup>™”, was obtained from BP Solar in December 2007. This sample is cut longitudinally from the original ingot similarly to the mc-Si slice. Examination of defects and impurities in this sample was performed based upon a MW-PCD minority carrier lifetime map. Structural defects and precipitates within the sample were examined using step-wise Secco etching combined with SEM and Nomarski microscopy. FT-IR was used to profile light element impurities and DLTS was used to profile metallic impurities. As with the cast mc-Si sample, minority carrier lifetime was observed to correlate with the DLTS determined iron concentration profile. The iron concentration profile was observed to correlate well with transitions in structural defect type. The structural defects observed suggest a vacancy and interstitial incorporation dependency on crystal growth parameters, as described by Voronkov, for silicon grown using the Czochralski method. Dissolved impurity concentrations within the Mono<sup>2</sup>™ ingot were found to be significantly higher than the mc-Si sample, despite having very similar casting parameters. This is perhaps due to a reduction in dislocations and grain boundaries that act as gettering sites. Precipitates were observed to nucleate rows of dislocations that extended in the direction of crystal growth. These rows of dislocations were observed to merge with other rows creating more densely packed rows termed “dislocation cascades”. These cascades are observed to branch and merge as crystal growth continues. Branching was observed to occur in the presence of oxide precipitation contaminated with metallic impurities.

Defect and Impurity Distributions in Traditionally Cast Multicrystalline and Cast  
Monocrystalline Silicon for Solar Substrates

by  
Ian Thomas Witting

A thesis submitted to the Graduate Faculty of  
North Carolina State University  
In partial fulfillment of the  
Requirements for the degree of  
Master of Science

Materials Science and Engineering

Raleigh, North Carolina

2008

APPROVED BY:

---

Carlton Osburn

---

Gerd Duscher

---

George Rozgonyi  
Committee Chair

## **DEDICATION**

I dedicate this thesis to my mother, Sylvia Lynn Witting, whose self-sacrifice and perseverance laid the path for her children's success.

## **BIOGRAPHY**

Ian Thomas Witting was born in Durham, North Carolina in 1983 to parents Thomas and Sylvia Witting. He received his B.S. in Materials Science and Engineering from the Cornell University College of Engineering in 2006. He enrolled in North Carolina State University under the guidance of George Rozgonyi in the Department of Materials Science and Engineering in 2006.

## ACKNOWLEDGMENTS

I would like to thank Dr. George Rozgonyi for accepting me to his program and helping me to gain valuable perspective on the relationship between industry and education. I am grateful to Dr. Magnus Wagener for his teaching and guidance in the laboratory. I wish to thank Nathan Stoddard of BP Solar for his supplying of samples discussed in this document and for his informative exchanges about my work. I want to extend thanks to Jinggang Lu, Xuegong Yu, and all other members of the Rozgonyi group for their advice and help around the lab.

I would like to acknowledge the NCSU Nanochemistry Laser and Vibrational Spectroscopy Laboratory for the usage of and Dr. Simon Lappi for his help with the FT-IR. I would like to also acknowledge the NCSU Analytical Instrumentation Facility and Chuck Mooney, Roberto Garcia, and Fred Stevie for help with the use of the SEM and SIMS.

My sincere thanks to Robert Quackenbush and William Whitmore for inspiring my interest in physics and chemistry, respectively. Without them I would have had no direction upon entering college. I want to thank Dr. George Whitesides for allowing me to be part of his research group at Harvard. I would like to thank George Kaufman for being the first to give me experience with research as well as being a great friend and mentor to me during my summers at Harvard. I would like to thank Dr. Abraham Stroock for giving me a chance to perform research in a field outside of my realm of experience.

# TABLE OF CONTENTS

LIST OF FIGURES .....	vi
METHODOLOGY .....	1
Introduction .....	1
Microwave Photoconductance Decay (MW-PCD) .....	1
Fourier Transform Infrared Spectroscopy (FT-IR) .....	2
Deep Level Transient Spectroscopy (DLTS) .....	4
Secondary Ion Mass Spectroscopy (SIMS) .....	6
Defect Delineation Etching .....	7
Other Methods .....	8
Figures .....	9
References .....	11
ANALYSIS OF TRADITIONALLY CAST MULTICRYSTALLINE SILICON SLICE AND THE CASTING ENVIRONMENT .....	13
Introduction .....	13
Materials and Methods .....	17
Results and Discussion .....	19
Conclusion .....	25
Figures .....	27
References .....	36
ANALYSIS OF CAST MONOCRYSTALLINE SILICON SLICE .....	39
Introduction .....	39
Materials and Methods .....	41
Results and Discussion .....	42
Conclusion .....	55
Figures .....	57
References .....	65
CLOSING REMARKS .....	67

## LIST OF FIGURES

### METHODOLOGY

Figure 1.	Schematic of a Michelson interferometer .....	9
Figure 2.	Example of a typical interferogram from an infrared glower .....	9
Figure 3.	Illustration of the rate window concept used in DLTS .....	10
Figure 4.	Correlation of etch pit features to crystalline defects .....	10

### ANALYSIS OF TRADITIONALLY CAST MULTICRYSTALLINE SILICON SLICE AND THE CASTING ENVIRONMENT

Figure 1.	Scan of multicrystalline slice with corresponding MW-PCD lifetime map .....	27
Figure 2.	Morphologies present on the top of a cast multicrystalline ingot .....	28
Figure 3.	Example FT-IR absorbance spectra for the 7 cm elevation sample .....	29
Figure 4.	FT-IR determined interstitial oxygen and substitutional carbon concentrations with distance from sidewall at 7 cm elevation .....	30
Figure 5.	MW-PCD scan of the FT-IR sample taken at 7 cm elevation .....	30
Figure 6.	FT-IR determined interstitial oxygen and substitutional carbon concentrations with distance from sidewall at 21 cm elevation .....	31
Figure 7.	MW-PCD scan of FT-IR sample taken at an elevation of 21 cm .....	31
Figure 8.	DLTS determined iron-boron complex concentration profile with elevation above crucible base .....	32
Figure 9.	Samples with surface contamination from different furnace environments .....	33
Figure 10.	SIMS data from CZ sample exposed to furnace used for baking release coating .....	34
Figure 11.	SIMS data from a second site on the contaminated CZ wafer .....	35

**LIST OF FIGURES (continued)**

**ANALYSIS OF CAST MONOCRYSTALLINE SILICON SLICE**

Figure 1.	Scan and MW-PCD lifetime map of monocrystalline sample .....	57
Figure 2.	Composite of Nomarski images showing transitions in defect type with elevation in Mono <sup>2</sup> ingot .....	58
Figure 3.	Sample DLTS Spectrum from 28.8 mm elevation .....	59
Figure 4.	DLTS determined Fe-B concentration with elevation in the Mono <sup>2</sup> ingot .....	59
Figure 5.	FT-IR absorbance spectra for monocrystalline sample .....	60
Figure 6.	FT-IR determined light element impurity concentration profiles in a monocrystalline ingot .....	60
Figure 7.	Composite of Nomarski images showing behavior of dislocation lines .....	61
Figure 8.	Nomarski images illustrating dislocation cascade branching .....	62
Figure 9.	Secondary electron image showing a dislocation cascade branching .....	63
Figure 10.	Dislocation cascades viewed from a plane parallel to the ingot base .....	63
Figure 11.	Comparison of interstitial oxygen levels with elevation in monocrystalline and multicrystalline ingots .....	64

## **METHODOLOGY**

### **Introduction**

There are three types of measurements that are used to evaluate material in this report: electrical, structural, and chemical. If the ultimate goal of this research is to produce better quality cast silicon for applications such as solar cells, we must first decide on a materials property to use as our determining factor between “good” and “bad” material. The property selected as the starting point in this study is minority carrier lifetime, an electrical measurement. If a given region of silicon has a low minority carrier lifetime, charge carriers generated by light absorption will recombine too quickly to be collected at electrodes in a solar cell thus giving reduced power generation. Once the lifetime of a given sample of silicon has been measured, the next step is to question why the lifetime is what it is. Correlation of the lifetime with structural information, such as crystal defects, and chemical information, such as impurity concentration, can lead to understanding lifetime measurements. Determining the sources of defects and impurities can lead to controlling them and improving future manufacturing methods. Described in this section are descriptions of the methods used for making electrical, structural, and chemical measurements performed in the chapters that follow.

### **Microwave Photoconductance Decay (MW-PCD)**

Microwave photoconductance decay (MW-PCD) is a contactless method for measuring the minority carrier lifetime in silicon. A map of measured lifetimes produced via MW-PCD can be used to identify “good” and “bad” regions of samples or for comparison of

samples before and after a given manufacturing process step. A MW-PCD lifetime map is used as the starting point for examination of chemical impurities and structural defects in the samples described in this report. Lifetime measurements are performed by monitoring the microwave reflectance of a sample while periodically exciting excess charge carriers. A laser pulse of light creates excess minority carriers that are observable through changes in microwave reflection. The transient decay in this reflection after an excitation pulse can be used to approximate the minority carrier lifetime. The lifetimes obtained by MW-PCD can only be considered effective lifetimes because of surface recombination contributions. In order to obtain lifetime values as close as possible to true bulk values, measurements are usually taken with the sample surface passivated either by immersion in a passivating solution or by growth of a passivation layer of oxide or nitride on the surface (Schroder 2006).

MW-PCD was performed using an Amecon Janus 300-M at NC State and a SemiLab WS2000 at BP Solar. The Janus 300-M is capable of measuring samples with a resistivity between  $0.1 \Omega\text{cm}$  and  $500 \Omega\text{cm}$  and lifetimes between 500 ns and 10 ms. MW-PCD scans performed at NCSU were taken using quinhydrone/methanol as a surface passivant (Takato et al. 2002). Scans performed at BP Solar were taken using iodine/methanol for surface passivation.

### **Fourier Transform Infrared Spectroscopy (FT-IR)**

Fourier Transform Infrared Spectroscopy (FT-IR) is a contactless optical transmission technique useful for the identification and quantification of light element impurities in

silicon. Spectrometers for FT-IR use a Michelson interferometer with a collimated beam from an infrared source. Figure 1 shows a schematic of a Michelson interferometer and the detected interference for a single wavelength source. A mirror in the interferometer is modulated back and forth over a small distance to create an interferogram in the measured light transmission through the sample chamber. An example of an interferogram for a continuous spectrum infrared source is shown in Figure 2. The highest resolution spectral data comes from the tail ends of the spectrum corresponding to the largest mirror displacement. A Fourier transform of the interferogram yields a spectrum with information about the source and anything else within the path of the beam. Spectra are converted to percentage transmission by taking the ratio of a spectrum with the sample in the beam to spectrum collected with an empty chamber. Absorbance spectra are calculated by taking the negative logarithm of percentage transmission data. Subtraction of an impurity free reference spectrum for silicon yields an absorbance spectrum for the sample containing only peaks corresponding to light element impurities at characteristic wavelengths. The height of a peak can be used to calculate the concentration of the impurity (Schroder 2006). Sample thicknesses and surface quality should be matched as closely as possible for reliable results.

FT-IR was performed on each sample at room temperature using a BioRad FTS-6000 spectrometer operating in transmission mode. Infrared light is focused onto the photodiode of a liquid nitrogen-cooled, wide band mercury-cadmium-telluride (MCT) detector with a normal spectral response of 450 to 7000  $\text{cm}^{-1}$ . The spectrometer and sample compartment are purged with nitrogen gas which reduces the possibility of atmospheric water or carbon dioxide contamination of the spectra and samples. Each reported spectra is the average of 64

scans. All spectra were recorded at room temperature with a resolution of  $2\text{ cm}^{-1}$ . Data is collected using the Win-IR Pro software package and processed using Microsoft Excel. Measurements were taken using a 5 mm square aperture in 5 mm steps along the length of each sample. The silicon reference sample used was a float zone sample provided by MEMC. Interstitial oxygen concentration and substitutional carbon concentration were calculated from observed spectra according to ASTM Standards F1188 and F1391, respectively (ASTM Standards 2002, 2000).

### **Deep Level Transient Spectroscopy (DLTS)**

Deep Level Transient Spectroscopy (DLTS) is a technique used to measure the concentration and identity of recombination centers at energies within the band gap of silicon. The fabrication of Schottky diodes is necessary for performing measurements. During measurements, a diode is held at a constant reverse bias and pulsed with a reduced bias. The magnitudes of these biases can be used to select the depth for probing as the width of the space charge region in the diode varies with applied voltage. When the diode is held in reverse bias, the space charge region is at its widest and depleted of majority carriers. During a pulse, majority carriers move into the previously depleted region filling some traps along the way. Once the diode is returned to the reverse bias state, free majority carriers move quickly out of the space charge region. Traps emit previously captured majority carriers and the total concentration of occupied traps decays exponentially by a characteristic time constant for each type of trap. This emission can be observed by monitoring the transient change in capacitance of the diode. The time constant of the capacitance decay

decreases with increasing temperature so some traps may empty too quickly to be measured at room temperature. For this reason, DLTS data is collected over a range of temperatures ranging from room temperature down to cryogenic temperatures.

A rate window is selected during DLTS spectrum collection that sets two time points in the transient decay at which to measure the capacitance. A plot of the difference in the capacitance at these two time points versus temperature is the DLTS spectrum. At sufficiently high temperatures, a given trap may empty too quickly after a pulse to be measured. The decay thus happens before the rate window so the change in capacitance is zero. At sufficiently low temperatures, a trap empties too slowly to produce a measurable change in capacitance during the rate window so the change in capacitance is zero in this case as well. Between the high and low temperatures, a measurable change in capacitance over the rate window is observed. A plot of this capacitance difference produces a DLTS spectrum as shown in Fig. 3.

The position of peaks in a DLTS spectrum is related to the identity of the trap, and the height of the peak is related to the trap concentration (Schroder 2006). Samples were selected from near the base of the ingot for DLTS measurements. In order to avoid interfering signals from extended defects, the samples were Secco etched for 1 minute to reveal grain boundaries or areas of high dislocation density so that they could be avoided during measurement (d'Aragona 1972). A thin oxide was grown on the samples using an equal parts mixture of hydrogen peroxide and sulfuric acid. Aluminum contacts of 1 mm diameter were evaporated on the samples to form Schottky diodes. DLTS was performed on these samples over a temperature range of 30K to 300K.

## **Secondary Ion Mass Spectroscopy (SIMS)**

Secondary ion mass spectroscopy (SIMS) is a method used for chemical identification and concentration quantification of elements present in a sample. A sample is hit with an ion beam to destructively remove material. Since material is removed, data obtained is a concentration profile with depth. Ejected atoms from the sample are analyzed in a mass spectrometer and identified by the ratio of their mass to their charge. Concentration of atoms in the sample is related to the detection count per unit time of a given element. Neutral atoms cannot be detected, and not all atoms ejected are ionized. In addition, a given element may ionize at different rates depending on the matrix it is present in. For these reasons, known standards are necessary to obtain accurate concentrations from count per time data. For example, the quantification of iron in a silicon sample requires comparison with a standard silicon sample with a known iron contamination level (Schroder 2006).

SIMS was performed on one sample at the NCSU Analytical Instrumentation Facility using a Cameca IMS 6f using an  $O_2^+$  beam running at 5.5 kV with an incidence angle of 42 degrees from normal. Beam current was maintained at 80 nA. The beam raster area was 180  $\mu\text{m}$  squared and ions were detected from a 30  $\mu\text{m}$  region in the center of the raster. The only standard used for comparison was iron in silicon. Thus, the only element with a known concentration profile is iron. All other elements present in the SIMS data is shown for qualitative determination and concentrations should not be considered accurate.

## **Defect Delineation Etching**

Defect delineation etching is a powerful technique used for the detection and identification of structural defects such as dislocations. All silicon etchant solutions are composed of three basic components: an oxidant, hydrofluoric acid, and a rate controlling buffer. The oxidant creates silicon dioxide on the surface of the sample and the hydrofluoric acid strips this oxide away. The ratio of these components determines whether the etchant solution will result in delineation of defects or polishing of the surface. If the hydrofluoric acid is sufficiently dilute that it cannot immediately remove oxidized silicon, etching will be limited by the transport of HF to the surface. The etch rate will thus be higher at surface regions that have a high radius of curvature. Such an etching solution can be used for chemical polishing of the surface. If instead the oxidation is the rate limiting step, the etch rate will be determined by the oxidation rate for a given location on the sample surface. Differences in the oxidation rate caused by defects at or beneath the sample surface will result in hills or pits being formed during etching. The size and shape of a given pit can be correlated to a specific crystalline defect as shown in Figure 4.

An ideal etchant would be isotropic, meaning it would expose defects equally well regardless of the sample surface orientation. Its effectiveness would be insensitive to the doping type (n or p) of the silicon sample and most importantly have a one-to-one correlation between observed etch pit and defect. No etchant is truly ideal, but the one described by D'Aragona, called the Secco etch, has proven to be the closest of the common etching solutions to an ideal one (Schimmel, 1976). Both polishing and defect delineation etchants were used in experiments described in this document. Polishing of FT-IR samples was

performed using a 2:1:1 mixture of nitric, hydrofluoric, and acetic acids, respectively. Defect delineation etching was performed using Secco etchant for various time durations (Secco D'Aragona 1972).

### **Other Methods**

Scanning electron microscopy (SEM) images were taken of as received samples from the top of a typical multicrystalline ingot grown by BP Solar using a Hitachi S-3200 SEM. Energy dispersive spectroscopy (EDS) was performed on features of interest with an Oxford Isis EDS system. EDS identifies elemental composition of features in an SEM by analyzing x-rays given off by a sample after collision with high energy electrons. Each element gives off x-rays of characteristic energy levels due to transitions of electrons excited by the SEM electron beam dropping to lower energy levels. This method is not incredibly sensitive and only resolves elements present in concentrations greater than 1%. Quantification using EDS is difficult and requires calibration with known standards and it does not provide information about the structure or exact stoichiometric composition of an observed phase. Despite these shortcomings, it is a useful qualitative tool for quickly and easily identifying the presence of elements in a sample.

## Figures

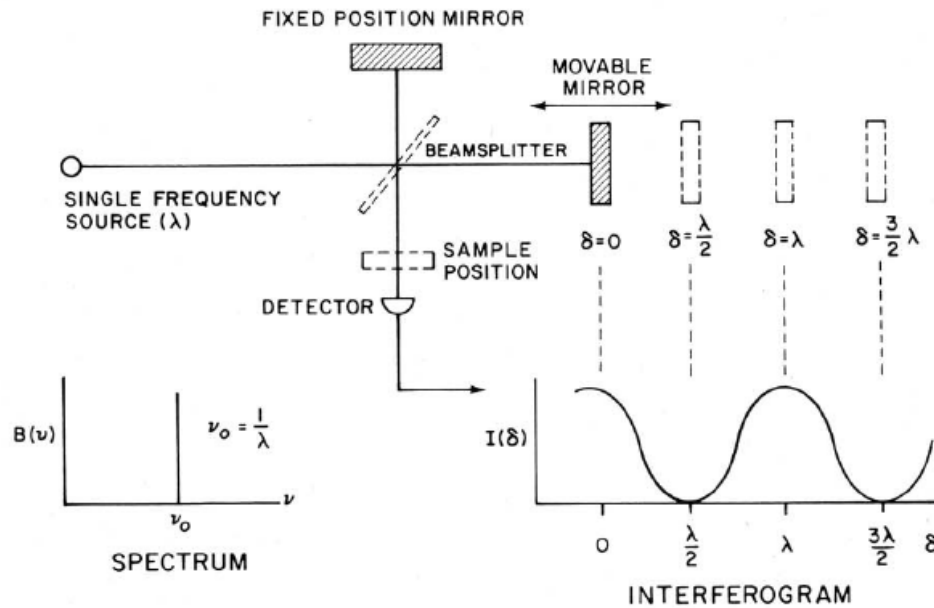


Figure 1: Schematic of a Michelson interferometer. The diagram at the bottom right demonstrates the interference pattern produced via translation of the movable mirror for a single wavelength source shown at the bottom left. (Figure from Perkins, 1986)

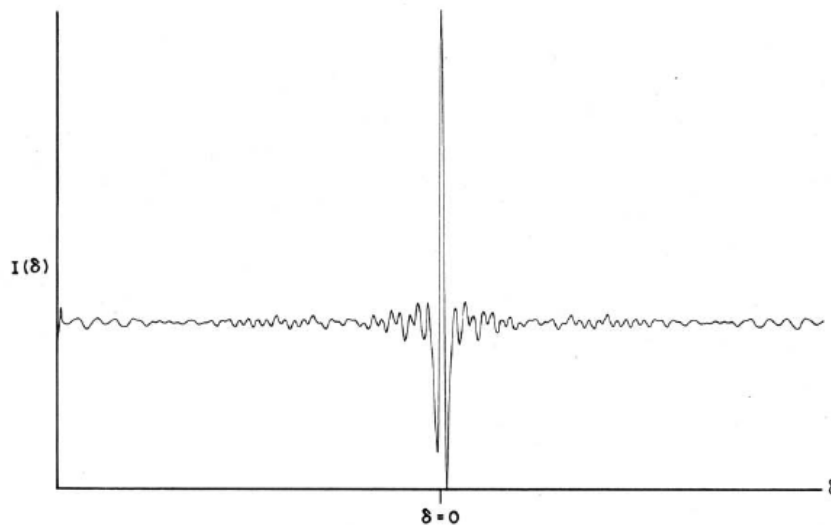


Figure 2: Example of a typical interferogram from an infrared glower. Intensity varies with mirror displacement,  $\delta$ . All frequencies constructively interfere at zero displacement which results in the large centerburst. The highest resolution spectral data is contained at the greatest mirror displacements. (Figure from Perkins, 1986)

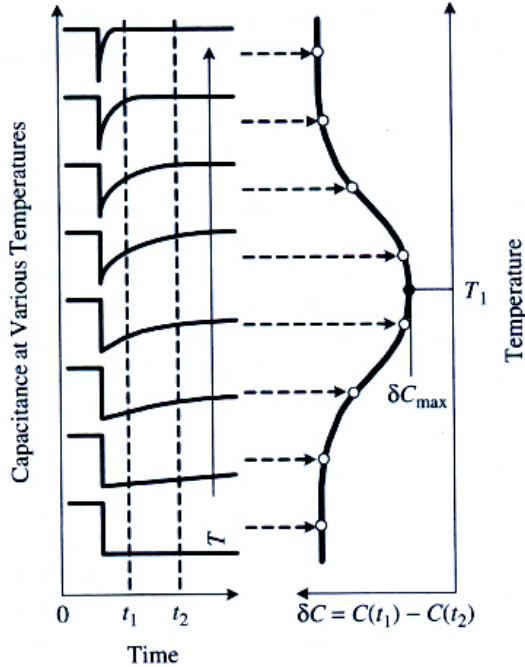


Figure 3: Illustration of the rate window concept used in DLTS. Two times,  $t_1$  and  $t_2$ , are arbitrarily chosen to define the rate window. The trap emptying transient has a time constant which varies with temperature. The change in capacitance from  $t_1$  to  $t_2$  for this transient,  $\delta C$ , is plotted versus temperature to produce the DLTS spectrum. (Figure from Schroder, 2006)

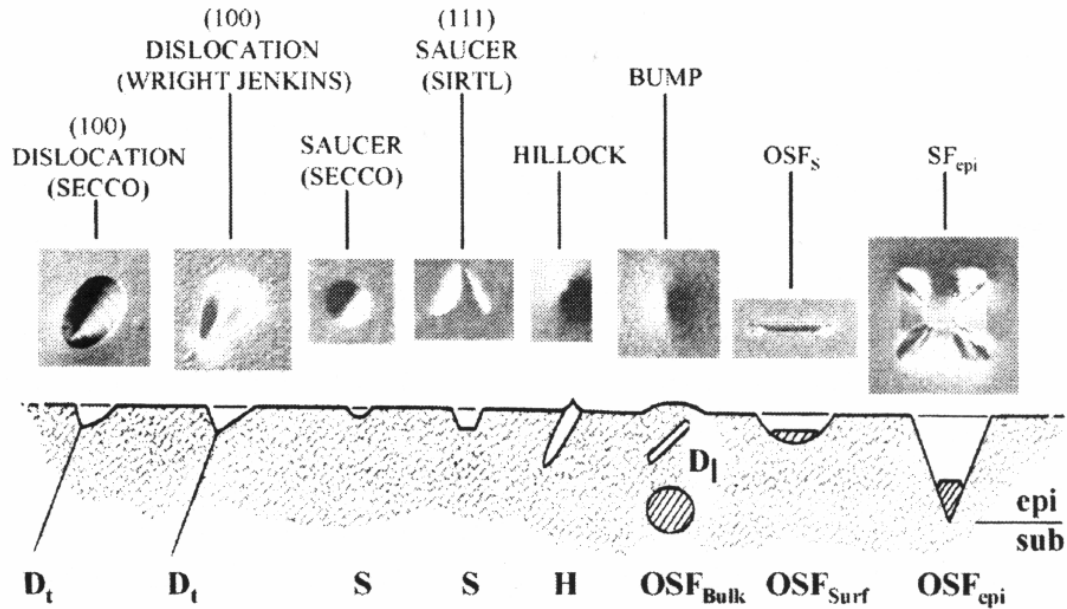


Figure 4: Correlation of etch pit features to crystalline defects. Different etchants will produce different etch pits for the same defect. Some etches are more useful for the identification of specific defect types. (Figure from Schroder, 2006)

## REFERENCES

**Takato, H., Sakata, I., & Shimokawa, R. (2002).** Quinhydrone/methanol treatment for the measurement of carrier lifetime in silicon substrates. *Japanese Journal of Applied Physics*, 41, 870-872.

**Schroder, D. K. (2006).** *Semiconductor Material and Device Characterization - Third Edition*. Hoboken, New Jersey: John Wiley & Sons, Inc.

**ASTM International (2002).** F1188 – Standard test method for interstitial atomic oxygen content of silicon by infrared absorption with short baseline. *ASTM Standards*

**ASTM International (2000).** F1391 – Standard test method for substitutional atomic carbon content of silicon by infrared absorption. *ASTM Standards*

**Perkins, W. D. (1986).** Fourier Transform-Infrared Spectroscopy. *Journal of Chemical Education*, 63(1), A5-A10.

**Schimmel, D. G. (1976).** A Comparison of Chemical Etches for Revealing <100> Silicon Crystal Defects. *Journal of the Electrochemical Society*, 123(5), 734-741.

**Secco D'Aragona, F. (1972).** Dislocation etch for (100) planes in silicon. *Journal of the Electrochemical Society*, 119(7), 948-951.

## **CHAPTER 1: ANALYSIS OF TRADITIONALLY CAST MULTICRYSTALLINE SILICON SLICE AND THE CASTING ENVIRONMENT**

### **Introduction**

When comparing methods of energy production, often the most important factor in deciding which to use is the cost per unit energy. The cost per unit energy can be minimized through lowering the cost of production of this energy or by increasing the amount of energy produced through a more efficient process. The solar industry works to address both of these goals by reducing the cost of production of their units and by increasing the efficiency of their units. Solar cell efficiency is a measurement of how much of the incident absorbable light on a cell is converted into usable electric current. When photons within a proper energy range illuminate a solar cell and are absorbed, electron-hole pairs are generated. Current, and thus usable energy, is obtained when these free electrons and holes successfully reach opposing electrodes. The efficiency of a solar cell can be reduced through loss of light absorbance by reflection or through loss of free mobile charge carriers within the cell before they can reach the electrodes. The loss of free electrons and holes through recombination is enhanced by the presence of traps, which are defects or impurities present within or at the surface of the substrate.

Silicon is the dominant semiconductor in use as a substrate for photovoltaic cells because its natural abundance results in lower costs of materials. There are different methods of growing silicon crystals, each having its own advantages and drawbacks. Single crystal silicon grown using the Czochralski (CZ) method contains low concentrations of deleterious impurities and defects. Multicrystalline silicon (mc-Si) has significantly higher

concentrations of metallic impurities and extended defects. In addition to crystal purity and quality advantages, single crystal silicon also lends itself to surface texturing that reduces reflection and increases absorption in solar cells (Restrepo et al. 1976). Texturing processes work best on (100) oriented surfaces in silicon. The grains in mc-Si silicon are randomly oriented so texturing is less effective and does not provide the same increase in absorption as for (100) oriented single crystal wafers (Xi et al. 2004). Despite these disadvantages, mc-Si silicon has become the material of choice for large scale manufacturing of solar cells as it is significantly less expensive than CZ silicon to produce.

The majority of mc-Si silicon is grown using casting methods and the casting process is responsible for the presence of defects and impurities in this material. During casting, low-impurity content silicon feedstock is placed within a fused silica crucible and heated to its melting point of 1420 °C. Contrary to CZ growth, in traditional mc-Si casting there is no seed to initiate a desired orientation in the crystal solidifying from the melt. Instead, nucleation of solid phase silicon at random orientations occurs at numerous sites along the base of the crucible. These solid sites grow until they contact each other forming boundaries between them. The melt is cooled slowly from the base of the crucible allowing silicon solidifying from the melt to assimilate onto the grains beneath. This process results in large columnar grains and increases uniformity in the resulting wafers. Dislocations form at different densities from grain to grain due to thermal stresses within each grain and from stress points at grain boundaries. Impurities enter the liquid silicon from the slight dissolution of the crucible and also from the casting furnace environment. Solid state diffusion of impurities from the crucible occurs after contacting regions solidify but remain

at a high temperature.

Both structural defects and impurities have been shown to cause reduced minority carrier lifetimes and diffusion lengths, two measurements that relate to how well free charge carriers can reach solar cell electrodes. Electron Beam Induced Current (EBIC) studies have shown the recombination at grain boundaries correlates with the density of dislocations at the boundary. Small-angle grain boundaries and general (random) boundaries thus have the highest recombination activity. Impurity decoration or precipitation at grain boundaries can increase their recombination activity (Seifert et al. 1993). Relatively low amounts of iron contamination ( $10^{12} \text{ cm}^{-3}$ ) have been shown to greatly increase the recombination activity of small-angle grain boundaries (Chen et al. 2005). Minority carrier lifetime measurements on mc-Si silicon have shown that dislocation density is inversely proportional to minority carrier lifetime. Interstitial oxygen concentrations are elevated in grains with high dislocation density (Arafune et al. 2006). The typical metal impurities present in cast silicon are Fe, Ni, Co, Mo, Cr, and Cu and all generally exist in high enough concentrations to significantly reduce the minority carrier diffusion length, yet observed diffusion lengths exceed those predicted by the contamination concentrations. This is because most of the metal atoms form precipitates of low recombination activity or are distributed inhomogeneously across the ingot at sites like dislocations and grain boundaries (Istratov et al. 2003). If the impurity concentration is below a critical level, these regions can be recovered during junction formation and through hydrogen passivation (Cuevas et al. 1997, Pankove 1991). The most heavily contaminated regions of the ingot are the edges that were in direct contact with the casting crucible and the top of the ingot due to impurities segregating into the melt during

solidification. These regions are removed and discarded prior to processing the ingot into wafers.

The complex interactions between impurities, defects, crystal orientation, grain size, etc. create a crystal growth system difficult to study and understand in full. Previous work on such material has shown that all of these parameters can have an impact on the electrical performance of the material. The work presented in this chapter aims to take a more practical approach and determine which of these contributing factors has the most significant impact on the material's performance as a solar substrate and then to identify its source so that it can be eliminated in future manufacturing. The general trend observed in previous research is that impurity decoration of defects leads to a large increase in the recombination activity of those defects. The negative effects of resulting hybrid defects could thus be diminished if either the impurities or the defects could be reduced or even eliminated during the crystal growth process. Grain boundaries and dislocations present in cast silicon are difficult to control and a promising attempt at such control is discussed in detail in the next chapter. Impurities are introduced from the casting crucible and the furnace environment, both of which are possible to modify. For this reason, this chapter will focus on the impact of crucible originating chemical impurities on the electrical performance of the silicon substrate. Elimination of the most significant crucible-originating impurities would reduce the amount of silicon that must be removed from the ingot periphery prior to wafering. This would lower the overall cost of each wafer as less material would be lost as waste. In addition, elimination of these impurities would improve the electrical performance of the substrate and raise the efficiency of resulting solar cells.

## Materials and Methods

Multicrystalline wafers are cut parallel to the ingot base and thus individual wafers do not contain information about the impurity distribution with elevation in the ingot. In addition, samples used for experiments typically come from ingots that have had their periphery removed. They therefore do not contain the regions of highest impurity content and do not lend themselves to exploration of impurity distribution profiles. A cross-sectional slice of traditionally cast mc-Si silicon was obtained from BP Solar in April 2007. This slice was cut vertically from the original ingot and has intact the bottom, side, and top edges which were in contact with the crucible during casting. It is 2 mm thick, 25 cm tall, and extends 15 cm from the side edge ingot into the bulk of the ingot. A Microwave-Photoconductance Decay (MW-PCD) scan was taken for the original slice as well as the three FT-IR samples after chemical polishing. These lifetime maps were taken with the samples under quinhydrone/methanol solution for surface passivation (Takato et al. 2002).

Three samples for use in Fourier Transform Infrared (FT-IR) spectroscopy were cut from the slice parallel to the ingot base at elevations of 1, 7, and 21 cm as indicated in Fig. 1. These samples were approximately 2 cm tall and extended 12 cm from the edge of the ingot into the bulk. Each sample selected for FT-IR was chemically polished in a 2:1:1 mixture of nitric, acetic, and hydrofluoric acids respectively. The samples were dipped in dilute HF prior to FT-IR measurements to strip any remaining oxide. FT-IR was performed on each sample at room temperature using a BioRad FTS-6000. Measurements were taken using a 5 mm square aperture in 5 mm steps along the length of each sample. The silicon reference sample used was a Float Zone (FZ) sample provided by MEMC. Interstitial oxygen

concentration and substitutional carbon concentration were calculated from observed spectrum using ASTM Standards F1188 and F1391, respectively (ASTM Standards 2002, 2000).

Four 2 by 2 cm samples were prepared for Deep Level Transient Spectroscopy (DLTS). These samples came from positions corresponding to the mid-base, mid-sidewall, mid-top, and center of the ingot. In order to avoid interfering signals from extended defects, the samples were Secco etched for 1 minute to reveal grain boundaries or areas of high dislocation density so that they could be avoided during measurement (d'Aragona 1972). A thin oxide was grown on the samples using an equal parts mixture of hydrogen peroxide and sulfuric acid. Aluminum contacts of 1 mm diameter were evaporated on the samples to form Schottky diodes. DLTS was performed on these samples over a temperature range of 30K to 300K using a BioRad Digital DLTS System.

Scanning electron microscopy (SEM) images were taken of as received samples from the top of a typical mc-Si ingot grown by BP Solar using a Hitachi S-3200 SEM. Energy Dispersive Spectroscopy (EDS) was performed on features of interest with an Oxford Isis EDS system. Three samples were received from BP Solar in April 2008 that were exposed to different furnace environments used for the casting process and had different colored layers on their surfaces. One sample was exposed to the kiln used for baking the release coating onto the crucible. Two other samples were exposed to the casting furnace environment. All samples were examined using EDS and the sample exposed to the kiln was examined using Secondary Ion Mass Spectroscopy (SIMS) using a Cameca IMS 6f.

## **Results and Discussion**

A MW-PCD scan of the as received slice shown in Figure 1 revealed the expected regions of low lifetime at the periphery of the ingot. This low lifetime region is unlikely to be due to structural defects present on the outside of the ingot because such defects are distributed randomly from grain to grain. If this were the case, we would expect to see the occasional “good” grain at the edge. The low lifetime regions at the base and side are due to impurities diffused in from the casting crucible. As seen in the MW-PCD map, the average lifetime is highest just above the low lifetime region at the base and decreases gradually with elevation. This is attributable to segregation resulting in gradually increasing concentrations of impurities with increasing elevation. The last of the solidifying melt contains very high concentrations of impurities that cause the low lifetime region at the top of the ingot. The width of the low lifetime band at the top of the ingot is due to impurities at the top surface diffusing back down into the ingot before the ingot is cooled. The first goal would be to determine what impurities are present in significant concentrations. Next we would want to determine which impurities have the largest impact on the electrical properties of the silicon, and finally we would want to identify the source of these impurities so that they could hopefully be eliminated in future processing. What follows is such an analysis of the mc-Si casting process.

### *Impurity Identification*

The impurity concentration in the ingot is highest at the very top surface due to segregation during solidification. Three morphologies were found to be present on the top of a BP Solar mc-Si ingot as shown in Figure 2: apparently clean silicon (Figure 2A, 2B), branching features (Figure 2C, 2D), and a dark gray haze (Figure 2E, 2F). SEM images and EDS spectra were collected for each morphology. Figure 2B is an SEM image of the clean appearing silicon showing the presence of numerous precipitates ranging in size from 1-10  $\mu\text{m}$  that were identified by EDS as iron silicide. These precipitates occur both within and between grains. The branching features are shown by EDS to be a combination of two different impurity precipitates. The needlelike features of Figure 2D are identified as silicon nitride and the mounds from which they emerge were revealed to be silicon carbide. The hazy regions are a crust of silicon carbide as shown in Figure 2F. It is likely that the iron precipitates are present over the entire top surface of the ingot but are masked by the carbide and nitride features. The primary impurities in the cast mc-Si material are carbon, iron, nitrogen, and oxygen and their effect on the minority carrier lifetime needs to be determined.

### *Determination of Impurity Significance*

FT-IR was performed on regions to determine if any light element impurities (C, N, O) are the cause of the low lifetime regions on the sides and base of the ingot. A sample of two FT-IR absorbance spectra is shown in Figure 3. The substitutional carbon peak is visible at  $605\text{ cm}^{-1}$  and the interstitial oxygen peak is visible at  $1107\text{ cm}^{-1}$ . Nitrogen and oxy-nitride peaks were not observed at their expected location between the carbon and oxygen peaks.

From the previous observations of the ingot top and from the knowledge that the release coating present between the ingot and crucible contains silicon nitride, nitrogen must be present within the bulk of the ingot. The FT-IR absorption of nitrogen related complexes is weak and requires a sample thicker than the 2 mm thick samples used in this study.

Exploring the nitrogen distribution is a possible route for future experiments. Oxygen and carbon distributions were obtained at three elevations in the ingot. Concentration profiling was performed at 5 mm intervals with distance from the crucible sidewall. MW-PCD scans were also taken of each sample used in FT-IR in order to determine if there is any correlation between the light element impurity concentrations and minority carrier lifetime. At 1 cm above the base of ingot, the interstitial oxygen concentration was found to have an average value of  $4.5 \times 10^{17} \text{ cm}^{-3}$  and did not seem to vary in any significant way laterally along the base of the ingot. The minority carrier lifetime does not vary laterally either since the impurity contribution from the base obscures the effects of impurities from the side.

At an elevation of 7 cm, the FT-IR determined interstitial oxygen concentration shown in Figure 4 drops steeply from an initial value of  $2.9 \times 10^{17} \text{ cm}^{-3}$  and levels to a near constant value of  $1.3 \times 10^{17} \text{ cm}^{-3}$  within 2 cm from the ingot edge. The substitutional carbon concentration profile at this elevation is flat and has an average value of  $1.0 \times 10^{17} \text{ cm}^{-3}$ . The MW-PCD determined minority carrier lifetime map is shown in Figure 5 and plotted graphically in Figure 4. The minority carrier lifetime is below detection level for 3 cm from the ingot edge and rises steeply to near  $4 \mu\text{s}$  between 3 and 4 cm from the edge. Beyond 4 cm from the edge of the ingot, the lifetime rises gradually to a value of near  $8 \mu\text{s}$  at a distance of 10 cm from the edge. From Figure 4, a direct comparison of the minority carrier lifetime

with the interstitial oxygen and substitutional carbon concentration profiles shows that a shift in the concentration of these elements does not correlate with a shift in lifetime.

FT-IR determined interstitial oxygen and substitutional carbon levels at an elevation of 21 cm showed slightly different spatial variations than those in the 7 cm sample. Shown in Figure 6, the interstitial oxygen is nearly constant with distance from the ingot edge and has an average value of  $1.0 \times 10^{17} \text{ cm}^{-3}$ . Similarly the substitutional carbon concentration also has flat concentration profile with an average value of  $5.4 \times 10^{16} \text{ cm}^{-3}$ . The MW-PCD determined minority carrier lifetime map for this sample is also shown in Figure 7 with a corresponding plot in Figure 6. The minority carrier lifetime is below detection level for a distance of 1 cm from the ingot edge before an abrupt rise to near  $4 \mu\text{s}$ . The minority carrier lifetime remains relatively constant between 1.5 and 8.5 cm from the ingot edge before making another steep rise to near  $8 \mu\text{s}$  at 9 cm from the ingot edge. There is no observable shift in interstitial oxygen or substitutional carbon concentration with distance and thus neither impurity correlates with the shift observed in the minority carrier lifetime. Carbon and oxygen are therefore either not the cause of the low lifetime band or their effects are completely masked by another impurity or defect.

DLTS was used to profile the iron concentration with distance from the base of the ingot to determine if it is the cause of the low lifetime regions at the ingot edge. The iron-boron complex concentration profile is shown in Figure 8. The concentration varies from  $4.7 \times 10^{12} \text{ cm}^{-3}$  at an elevation of 0.2 cm and remains fairly constant until an elevation 1.2 cm where it begins to drop gradually to  $2 \times 10^{12} \text{ cm}^{-3}$  at an elevation of 2.3 cm. Beyond this elevation the iron-boron concentration drops below our detection level of  $1.5 \times 10^{12} \text{ cm}^{-3}$ . The

corresponding minority carrier lifetime plot is also shown in Figure 8. The rise in lifetime with elevation corresponds well with the drop in iron-boron concentration suggesting that iron originating in the casting crucible is responsible for the low lifetime bands on the bottom and sides of the ingot. This result fits well with previously published data that shows that an FeB concentration of  $10^{12} \text{ cm}^{-3}$  would reduce the minority carrier lifetime to a maximum possible value of  $10 \mu\text{s}$  in the absence of other defects (Istratov et al, 2000). Iron is not present in the feedstock, the release coating, or the crucible in any appreciable concentration initially so it must be introduced during processing. Determining the source of the iron can lead to its elimination and the improvement of future manufacturing.

#### *Determination of Impurity Sources*

In order to determine the source of iron in the casting process, three samples were exposed to different furnace environments and the resulting surface contamination was analyzed using EDS and SIMS. Shown in Figure 9 are photos of these three samples. A large brick of mc-Si silicon was exposed to the casting furnace environment and a slight green haze was formed on its surface. A chunk of this brick was taken for examination and is shown in Figure 9A. A CZ wafer was subjected to the environment of a furnace used to bake the release coating onto the crucible prior to casting. An olive green coating was formed on the surface as shown in Figure 9B. A piece of feedstock was partially melted in the casting furnace environment and during this process a dark coating formed on the surface as seen in Figure 9C. All of the samples were examined within the SEM by EDS. The slight green haze on the sample exposed to the casting furnace environment was found to contain

C, O, and Fe. The feedstock piece was observed by SEM as shown in Figure 9D that strongly resembled the surface features shown in 2F. EDS identified this as carbide for both surface layers. The CZ sample only returned oxygen when analyzed by EDS. SIMS was performed to determine if any elements were present below the detection level of EDS and the results are shown in Figures 10 and 11. The elements detected in this surface layer are calcium, chromium, iron, potassium, and vanadium. The iron levels were compared to a standard, but no other elements were. Therefore, only the iron concentrations are truly quantitative and all other elements are only shown for qualitative purposes. The oxide deposited on the surface of the CZ wafer contains iron on the order of  $10^{19} \text{ cm}^{-3}$  and iron diffused into the wafer is found at a concentration around  $10^{18} \text{ cm}^{-3}$ .

Oxygen is higher at the periphery of the ingot because of solid state diffusion after solidification but before the ingot cools. This is supported by the oxygen concentration profiles shown in Figures 4 and 6. In Figure 4, the oxygen is shown to decrease with distance from the ingot edge and level off to a bulk value two centimeters from the ingot edge. In Figure 6, taken from a higher elevation, no significant drop in oxygen is observed. This means that if there is an elevated oxygen level near the ingot edge, it drops off to bulk levels within the first 5 mm from the crucible. The higher elevations in the ingot are solid and at elevated temperatures for a shorter duration than the lower elevations. The bulk values of oxygen are affected by oxygen dissolving into the melted silicon from the crucible and from the casting furnace as evidenced by the surface contamination on samples exposed to its environment. Carbon does not vary significantly with distance from the crucible which is supported by the lack of a large amount of carbon present on the surface of the CZ sample

exposed to the crucible baking furnace. Thus the carbon level in the ingot is affected almost exclusively by the casting environment. This carbon must enter the ingot through the melted silicon during casting.

The casting environment does contribute iron, but this is not the cause of the low minority carrier lifetime band at the bottom and sides of the ingot. The casting furnace can contribute iron to the melted silicon and to the top of the ingot immediately after solidification. Iron in the melted silicon will raise the bulk values of iron in the ingot, but much of this iron will segregate to the ingot top. Iron deposited on the top of the ingot post solidification will raise the iron level of the silicon just beneath the top surface, but would probably be negligible to the large amount of iron that segregates to the top of the ingot and diffuses back down. This is supported by the large iron precipitates observed on the top as shown in Figure 2B which were formed during solidification. The iron that is responsible for the low lifetime band at the sides and base of the ingot comes from the furnace used to bake the release coating onto the crucible. Iron on the order of  $10^{19} \text{ cm}^{-3}$  is deposited on the crucible surface and also high amounts would diffuse into the crucible during this process. This would add considerable amounts of iron to the bulk of the ingot and clearly to the ingot periphery.

## **Conclusion**

The work presented in this chapter has taken a perspective not typically seen in other work on mc-Si silicon. The sample used was cut vertically from a traditionally cast ingot and had intact the most heavily contaminated regions of the original ingot. The reduction in

minority carrier lifetime at the ingot periphery was found to be due to crucible originating iron contamination and not carbon or oxygen. This iron along with other metallic impurities was found to be introduced into the crucible during the kiln firing of the release coating onto the crucible. Additional iron was found to be introduced into the bulk of the silicon ingot by the casting furnace itself. Carbon enters the ingot from the casting furnace at such high levels that it produces a visible coating on some feedstock pieces during the melting process. Oxygen enters the ingot from the silica crucible. These results are significant because they indicate the most significant impurities in mc-Si silicon are introduced during manufacturing and which processes introduce each specific impurity.

## Figures

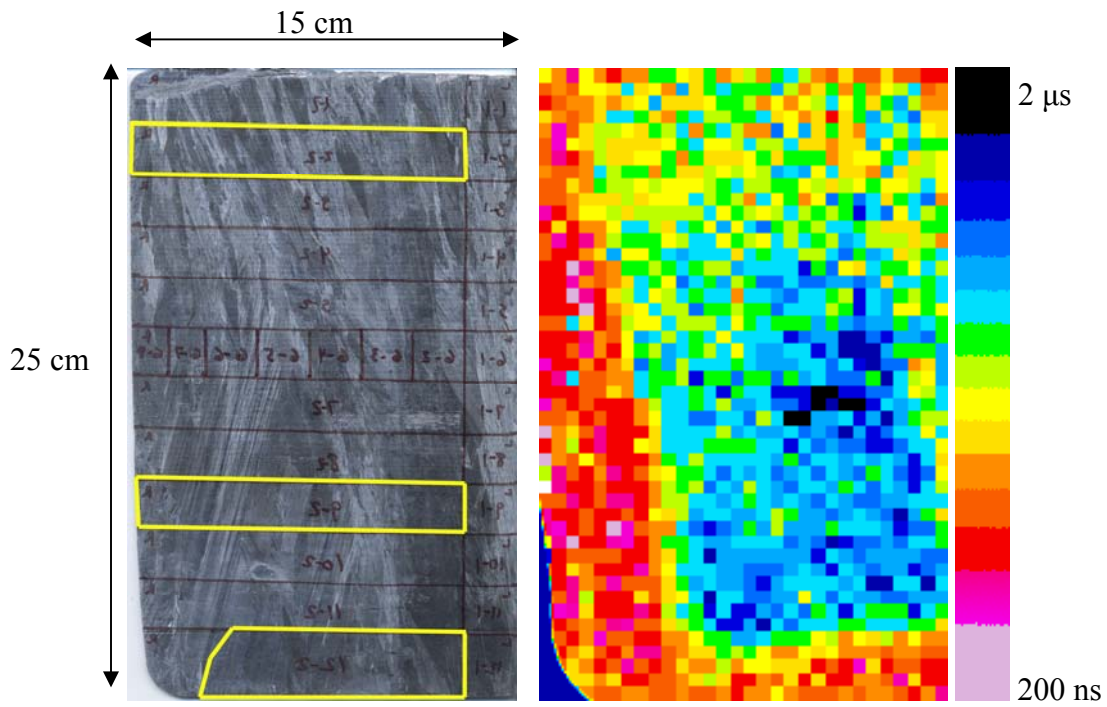


**Figure 1: Scan of multicrystalline slice with corresponding MW-PCD lifetime map. At left, a scan of the multicrystalline slice. Samples used for FT-IR measurements are outlined. At right: MW-PCD lifetime map of the original uncut slice. The low lifetime band at the side and base is visible**

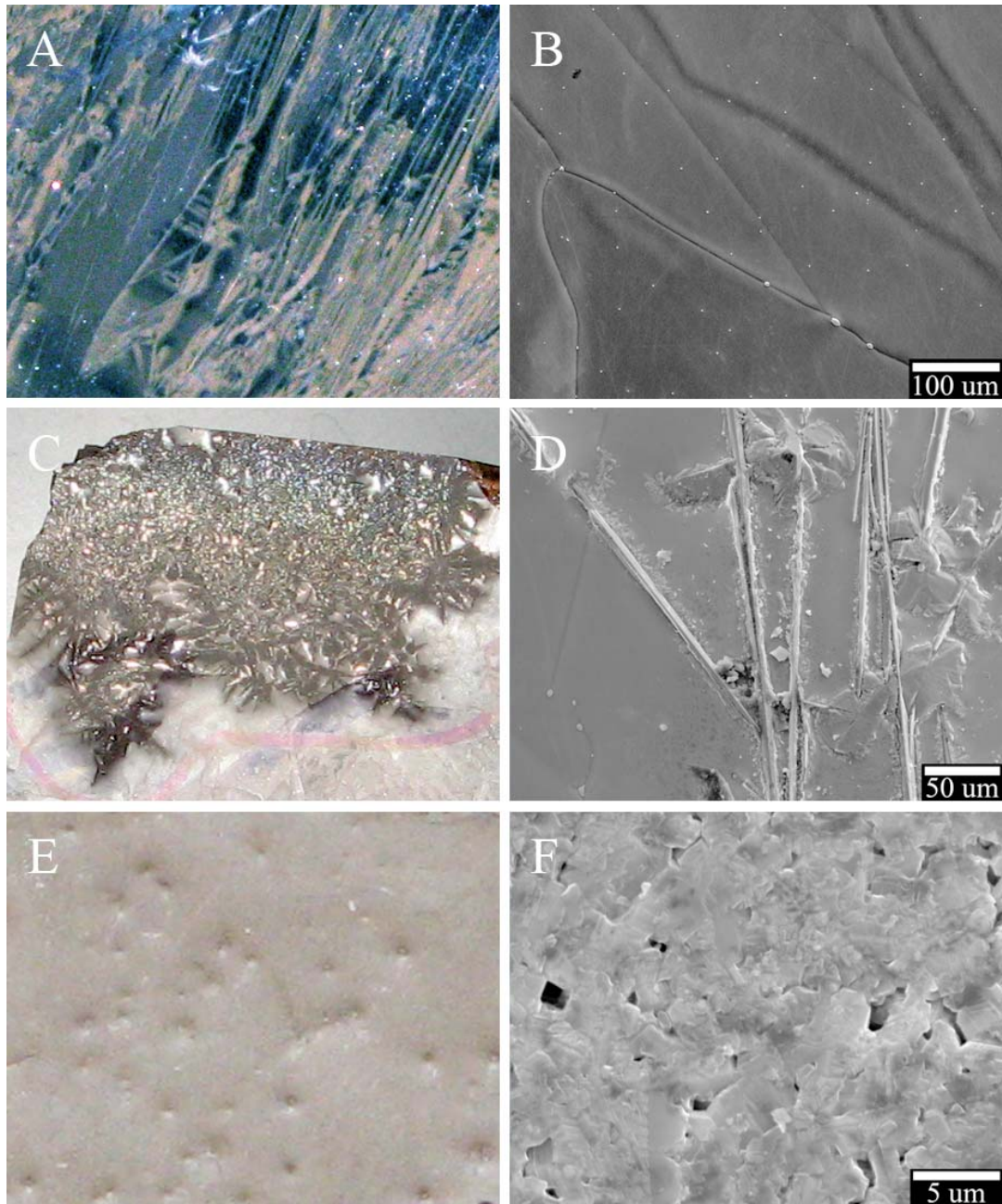


**Figure 2: Morphologies present on the top of a cast multicrystalline ingot. Image A is a photo of a seemingly clean region of the ingot top. Image B is a secondary electron SEM image of a similar region to image A that reveals precipitates at inter- and intragrain locations. EDS identifies these precipitates as iron silicide. Image C is a photo of “snowflake” features on the ingot top. Image D is a secondary electron SEM image of structures like those in C. EDS identifies the needle structures as silicon nitride and the mound structures as silicon carbide. Image E is a photo of a region covered in a gray haze with small bumps. Image F is a secondary electron SEM image of the region shown in E. EDS identifies the crust on the surface as silicon carbide.**

### FTIR Absorbance - 7 cm Elevation

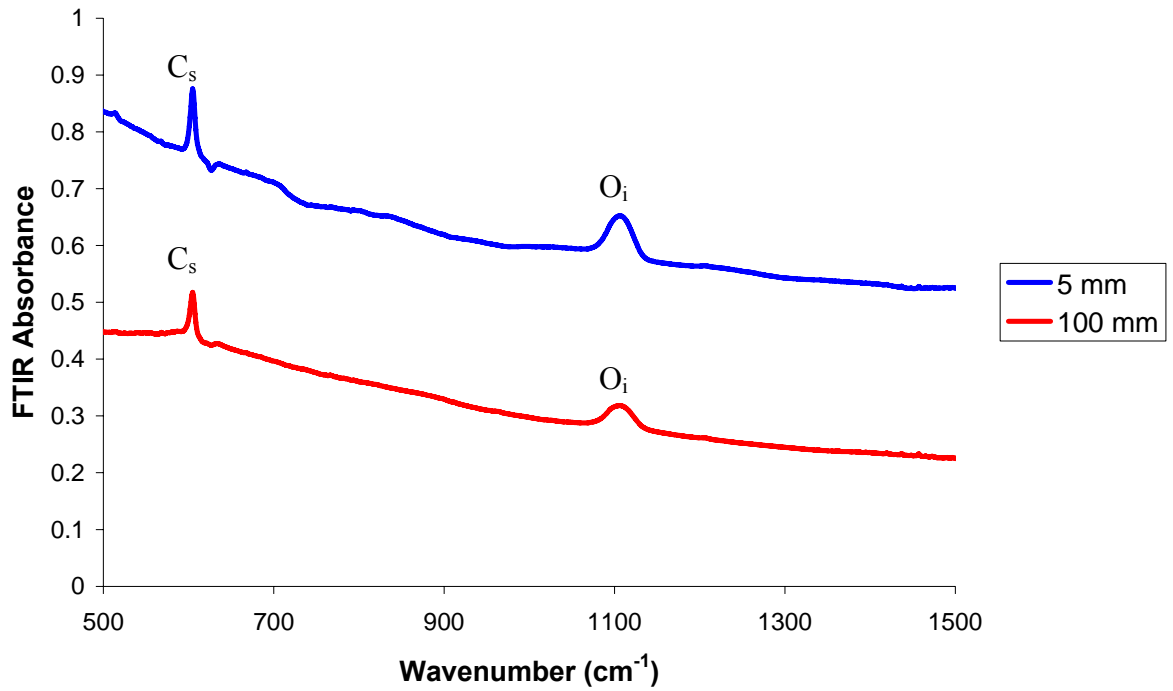


**Figure 3: Example FT-IR absorbance spectra for the 7 cm elevation sample. The FZ reference sample spectrum has been subtracted. The substitutional carbon peak is observed at 605 cm<sup>-1</sup> and the interstitial oxygen peak at 1107 cm<sup>-1</sup>. Both peaks are visibly smaller at 100 mm than at 5 mm away from the crucible wall.**

### FTIR Determined Light Element Concentrations - 7 cm

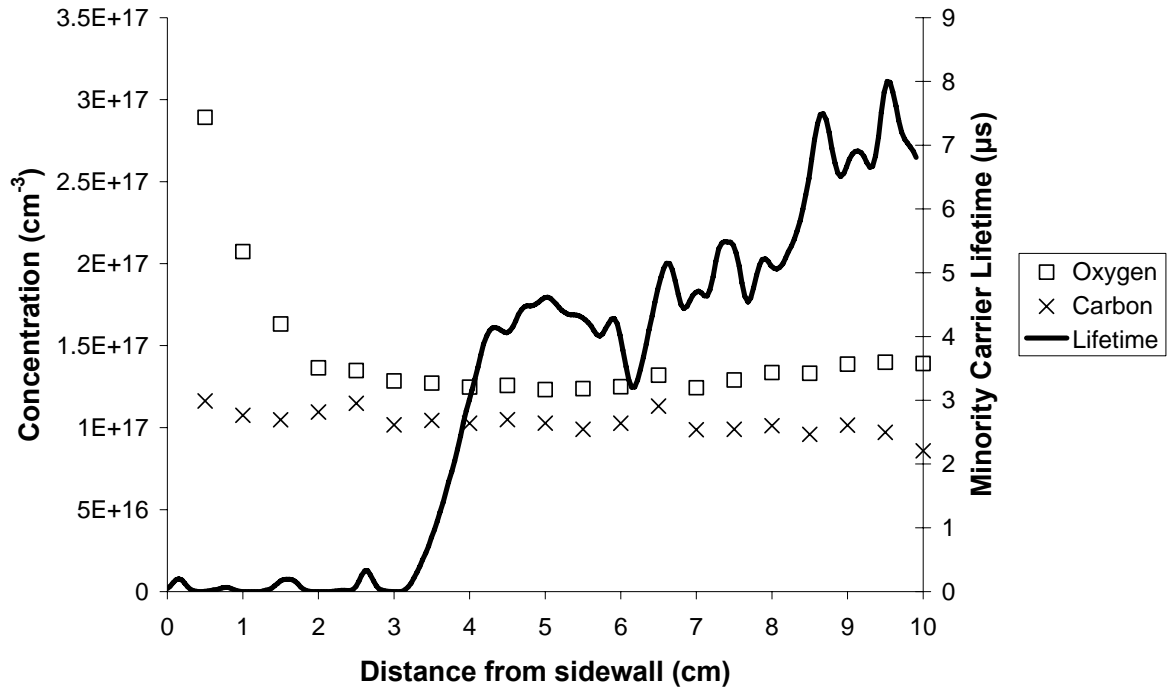


Figure 4: FT-IR determined interstitial oxygen and substitutional carbon concentrations with distance from sidewall at 7 cm elevation. Shown for comparison is the minority carrier lifetime for the same sample. Changes in oxygen and carbon are observed to not correlate with changes in lifetime.

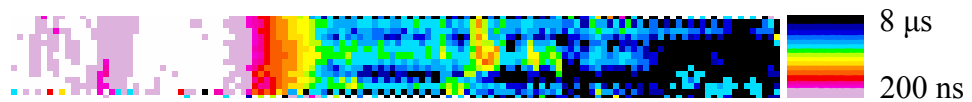


Figure 5: MW-PCD scan of the FT-IR sample taken at 7 cm elevation. The region closest to the crucible wall has a minority carrier lifetime below the 200 ns detection limit.

### FTIR Determined Light Element Concentrations - 21 cm

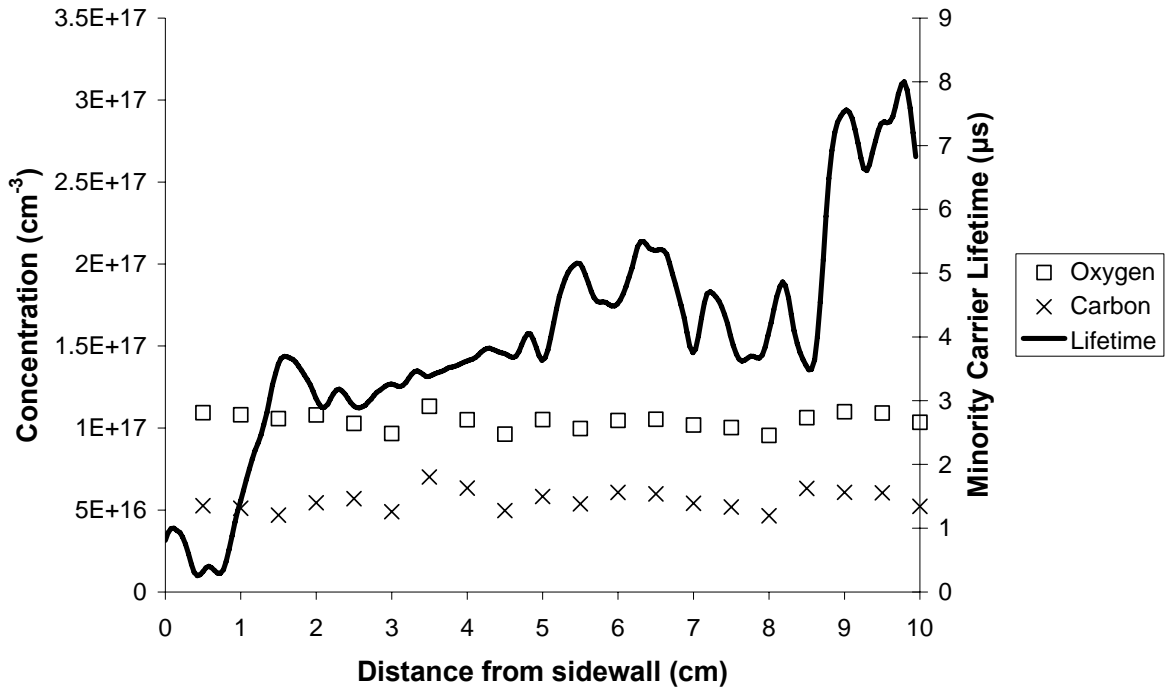


Figure 6: FT-IR determined interstitial oxygen and substitutional carbon concentrations with distance from sidewall at 21 cm elevation. Shown for comparison is the minority carrier lifetime for the same sample. Both oxygen and carbon concentration distributions are relatively flat. Changes in oxygen and carbon are observed to not correlate with changes in lifetime.

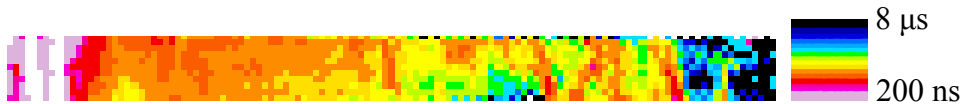
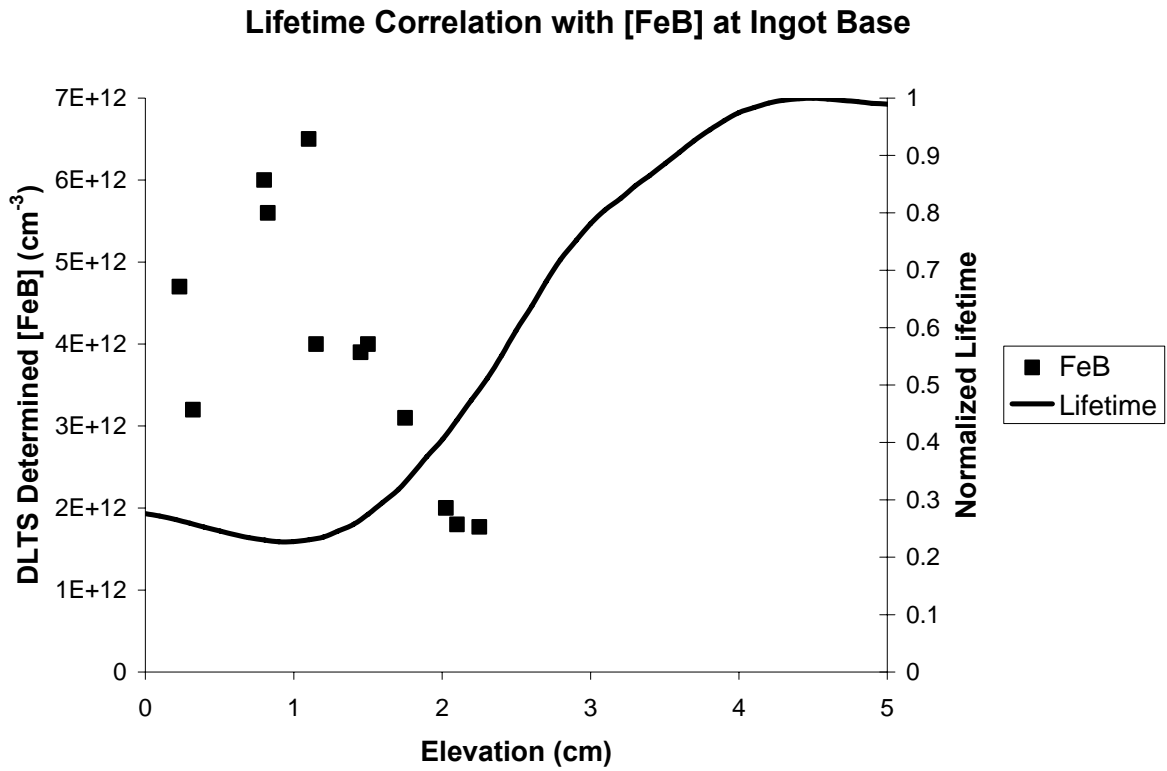
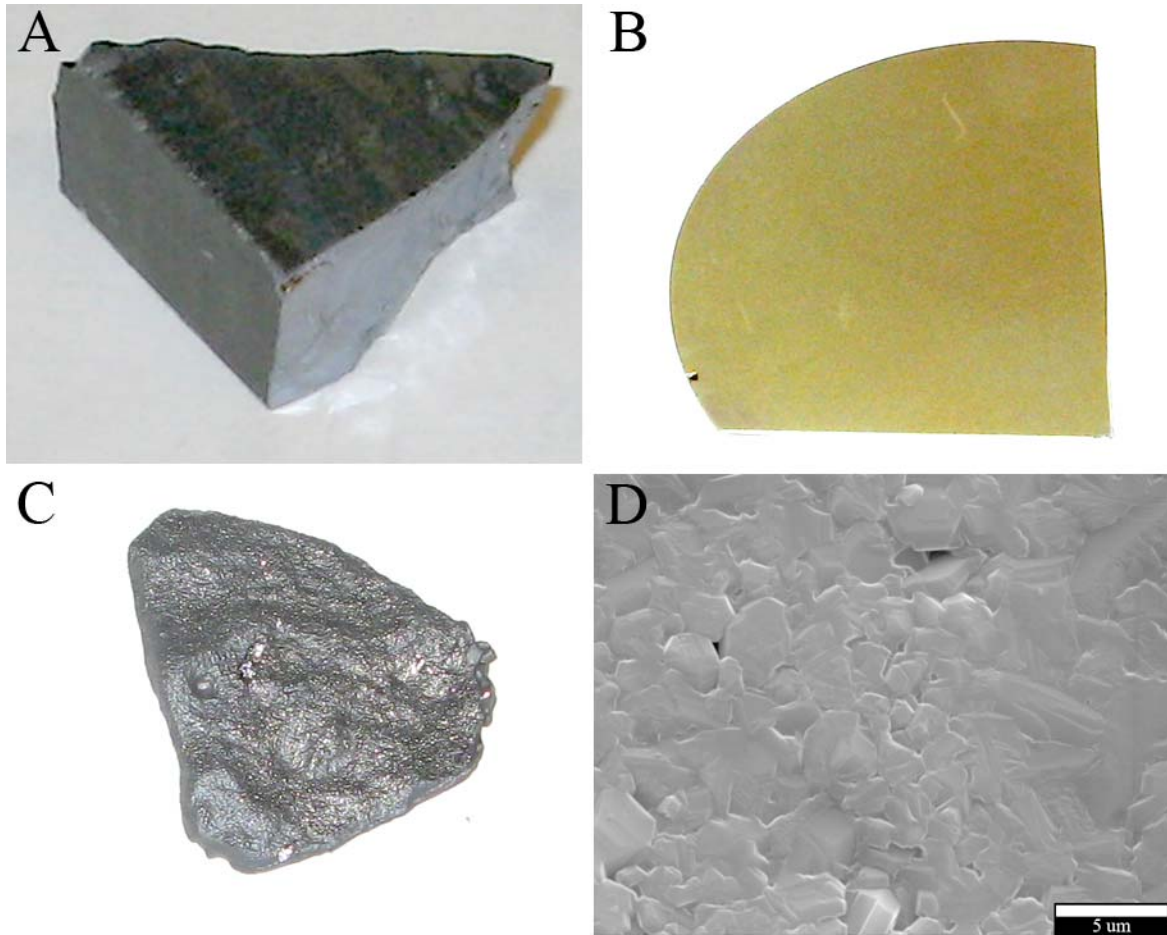


Figure 7: MW-PCD scan of FT-IR sample taken at an elevation of 21 cm. The low lifetime region near the crucible wall is thinner than in the 7 cm elevation sample.



**Figure 8: DLTS determined iron-boron complex concentration profile with elevation above crucible base. Shown for comparison is the minority carrier lifetime of this region as measured by MW-PCD. A drop in FeB concentration is observed to correlate with a rise in minority carrier lifetime.**



**Figure 9: Samples with surface contamination from different furnace environments. Image A shows a chunk of multicrystalline silicon subjected to the casting environment. A slight green haze is present on the top and left faces. Image B shows a CZ wafer piece exposed to a furnace used for baking a release coating onto the crucible. The oxide layer on the surface is fairly uniform and olive green in color due to its thickness of near 200 nm. Image C shows a piece of feedstock partially melted in a casting furnace. A dark coating is present on the surface. Image D is a secondary electron SEM image of the surface coating of the sample in Image C. EDS identifies this coating as carbide and its morphology is similar to that seen in Figure 2F.**

### CZ Sample SIMS Data Site 1

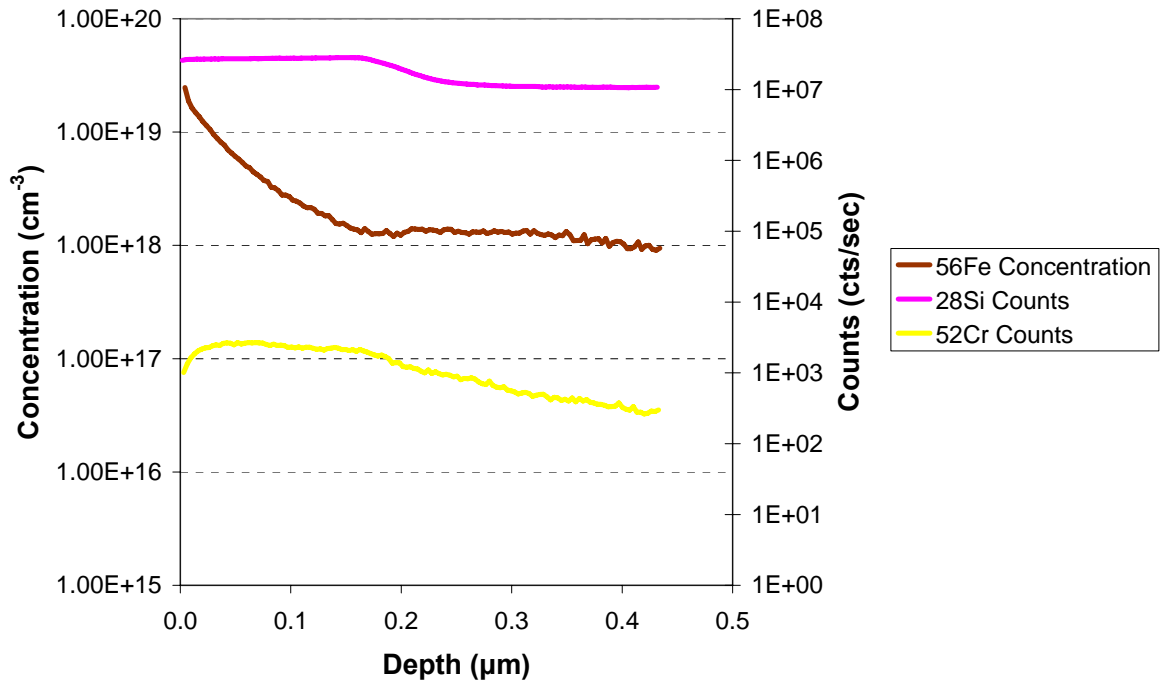


**Figure 10: SIMS data from CZ sample exposed to furnace used for baking release coating. Only Fe has been compared with a standard so only its concentration information is trustworthy. All other elements are shown for qualitative purposes.**

### CZ Sample SIMS Data Site 2

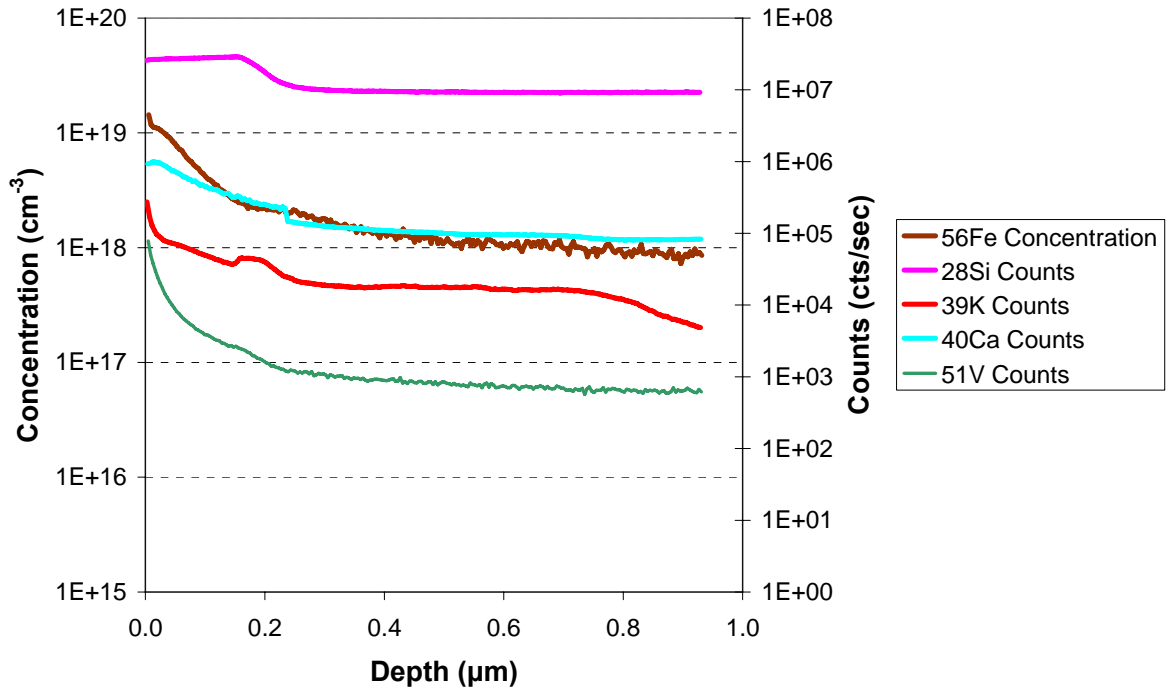


**Figure 11: SIMS data from a second site on the contaminated CZ wafer. Only Fe has been compared with a standard so only its concentration information is trustworthy. All other elements are shown for qualitative purposes.**

## REFERENCES

**Restrepo, F. & Backus, C. E. (1976).** On black solar cells or the tetrahedral texturing of a silicon surface. *IEEE Transactions on Electron Devices, Oct.*, 1195-1197.

**Xi, Z., Yang, D., Dan, W., Jun, C., Li, X., & Que, D. (2004).** Texturization of cast multicrystalline silicon for solar cells. *Semiconductor Science and Technology, 19(3)*, 485-489.

**Seifert, W., Morgenstern, G., & Kittler, M. (1993).** Influence of dislocation density on recombination at grain boundaries in multicrystalline silicon. *Semiconductor Science and Technology, 8*, 1687-1691.

**Chen, J., Sekiguchi, T., Xie, R., Ahmet, P., Chikyo, T., Yang, D., Ito, S., & Yin, F. (2005).** Electron-beam-induced current study of small-angle grain boundaries in multicrystalline silicon. *Scripta Materialia, 52*, 1211-1215.

**Arafune, K., Sasaki, T., Wakabayashi, F., Terada, Y., Ohshita, Y., & Yamaguchi, M. (2006).** Study on defects and impurities in cast-grown polycrystalline silicon substrates for solar cells. *Physica B, 376-377*, 236-239.

**Istratov, A. A., Buonassisi, T., McDonald, R. J., Smith, A. R., Schindler, R., Rand, J. A., Kalejs, J. P., & Weber, E. R. (2003).** Metal content of multicrystalline silicon for solar cells and its impact on minority carrier diffusion length. *Journal of Applied Physics*, 94(10), 6552-6559.

**Cuevas, A., Stocks, M., Armand, S., Stuckings, M., & Blakers, A. (1997).** High minority carrier lifetime in phosphorus-gettered multicrystalline silicon. *Applied Physics Letters*, 70(8), 1017-1019.

**Pankove, J. I. (1991).** Hydrogenation of Defects in Crystalline Silicon. In J. I. Pankove & N. M. Johnson (Eds.), *Hydrogen in Semiconductors* (pp. 35-47). San Diego, CA: Academic Press, Inc.

**ASTM International (2002).** F1188 – Standard test method for interstitial atomic oxygen content of silicon by infrared absorption with short baseline. *ASTM Standards*

**ASTM International (2000).** F1391 – Standard test method for substitutional atomic carbon content of silicon by infrared absorption. *ASTM Standards*

**Schroder, D. K. (2006).** *Semiconductor Material and Device Characterization - Third Edition*. Hoboken, New Jersey: John Wiley & Sons, Inc.

**Takato, H., Sakata, I., & Shimokawa, R. (2002).** Quinhydrone/methanol treatment for the measurement of carrier lifetime in silicon substrates. *Japanese Journal of Applied Physics*, *41*, 870-872.

**Secco D'Aragna, F. (1972).** Dislocation etch for (100) planes in silicon. *Journal of the Electrochemical Society*, *119*(7), 948-951.

**Istratov, A. A., Hieslmair, H., & Weber, E. R. (2000).** Iron contamination in silicon technology. *Applied Physics A*, *70*, 489-534.

## **CHAPTER 2: ANALYSIS OF CAST MONOCRYSTALLINE SILICON SLICE**

### **Introduction**

Monocrystalline silicon substrates result in higher efficiency solar cells than their multicrystalline counterparts because of their lower occurrences of trapping defects and because their surface can be well textured to reduce light reflectance. The most common method for growing single crystal silicon, Czochralski (CZ), is not without drawbacks. CZ silicon ingots are grown in round boules and the round wafers produced by these methods must be cut into “pseudo-squares”, squares with rounded corners, in order to fit into solar modules. This results in a loss of material and a loss of coverage on the final module and thus reduced power output for a given area. CZ silicon is also expensive to produce because it requires highly specialized equipment and monitoring by trained personnel. Cast multicrystalline silicon (mc-Si) is simpler and less expensive to fabricate. The cast ingots are square and wafers of this material are true squares and provide better coverage of the module surface. Solar cells produced from mc-Si material have lower efficiencies than those of single crystal substrates because of higher concentrations of trapping impurities and defects. In addition, the random orientations of the grains within mc-Si silicon do not lend themselves well to texturing. Multicrystalline silicon is currently the most widely used substrate for the production of solar cells because of its low cost and ease of production.

An ideal silicon substrate for solar cells would be single crystalline, square, simple and inexpensive to produce, and have low concentrations of trapping impurities and defects. BP Solar has been working towards these goals through the production of monocrystalline

cast silicon, termed Mono<sup>2</sup>™. This material is grown in the same fused silica crucibles used for traditional cast mc-Si silicon and utilizes the same furnaces. After preparing the crucible with a release coating, a seed crystal is placed at its base. Feedstock silicon is then loaded into the crucible and melted, but the seed crystal remains solid during this process. After all of the feedstock is melted, heat is removed from the base of the ingot through the seed. The liquid silicon slowly solidifies onto the seed taking the same crystallographic orientation. The resulting ingot is monocrystalline and square because of the shape of the crucible (Stoddard 2007).

This material shares properties of both single crystal silicon grown by the CZ method and cast mc-Si silicon. As with CZ silicon, the surface of Mono<sup>2</sup>™ wafers is (100) orientation, which makes them able to be textured. The wafers from these ingots do not contain grain boundaries and have a more uniform distribution of defects and impurities than observed in typical mc-Si wafers. As with cast mc-Si silicon, the periphery of the ingot is contaminated with impurities from the silica crucible and the furnace environment. There are some problems that are unique to Mono<sup>2</sup>™. Dislocation “cascades”, dense organized networks of dislocations, are present in the upper half of the ingot. These features can occur in CZ silicon as well but have been essentially eliminated in current methods of production. Casting is generally more tolerant of these features since the ingots produced this way are shorter making cascades affect less material that grows above them than in longer CZ ingots. These cascades branch and multiply with increasing elevation. Also, some mc-Si material exists near the sidewalls of the Mono<sup>2</sup>™ ingot and protrudes in further with increasing elevation (Stoddard et al. 2008).

The goal of the work presented in this chapter is to explore this new method of growing silicon by determining the types of defects and impurities present within this material and their distributions. It would be useful for the progress of this material to define just how similar Mono<sup>2</sup><sup>TM</sup> is to mc-Si cast silicon and CZ and also to better understand the dislocation cascades that are unique to it.

### **Materials and Methods**

A cross-sectional slice of a Mono<sup>2</sup><sup>TM</sup> ingot was obtained from BP Solar in December 2007. This slice is cut vertically relative to the ingot base and has intact the top and base of the ingot. The slice was cut approximately 2 cm from the sidewall of the ingot, and the original edge is not intact but some of the sidewall crucible impurities' contribution is visible in the minority carrier lifetime map. The slice is approximately 25 cm tall, 12 cm wide, and 2 mm thick and was received cleaved into pieces as shown in Fig. 1. Also shown in Fig. 1 is a Microwave Photoconductance Decay (MW-PCD) map of the uncleaved slice that was taken at BP Solar and supplied with the cleaved pieces.

Samples were selected for defect delineation etching with consideration of the MW-PCD lifetime map. These samples were polished and cleaned before etching. Step-by-step Secco etching was performed to reveal the nature of observed defects (Secco D'Aragona 1972). Etched samples were observed using Nomarski microscopy and a Hitachi S-3200 Scanning Electron Microscope (SEM). Features of interest in the SEM were identified chemically using an Oxford Isis Energy Dispersive Spectroscopy (EDS) system.

Samples were also selected for DLTS with consideration of the MW-PCD lifetime map. These samples were polished, cleaned, and stripped of oxide by dipping in dilute HF. A thin oxide layer was grown by immersing the samples in an equal parts mixture of hydrogen peroxide and sulfuric acid for 5 seconds. Aluminum contacts of 1 mm diameter were evaporated on the sample to form Schottky diodes. DLTS was performed over a temperature range of 300K to 30K using a BioRad Digital DLTS system.

Four samples were selected to obtain a light element concentration profile with elevation above the ingot base. These samples were selected from the slice to be as far as possible from the ingot side to reduce any contributions from the crucible sidewall. Each sample was chemically polished using a 2:1:1 mixture of nitric, acetic, and hydrofluoric acids, respectively. Fourier Transform Infrared (FT-IR) spectroscopy was performed on these samples at room temperature using a 5 mm square aperture. The reference sample used was a FZ sample supplied by MEMC. Prior to measurements, both the sample and reference were dipped in hydrofluoric acid to remove any surface oxidation. Data analysis was performed as described in ASTM F1188 and F1391 (ASTM Standards 2002, 2000).

## **Results and Discussion**

The exploration of defects and impurities begins with the MW-PCD lifetime map that provides a visual indication of regions of high charge carrier recombination activity which can then be correlated to structural and chemical results obtained from other experiments. Shown in Fig. 1 is a scan of the cleaved slice and the corresponding minority carrier lifetime map supplied by BP Solar of the original unclesaved sample. The primary

features visible in the MW-PCD map are a wide low lifetime band at the base, a low lifetime band at the side with grain boundaries visibly encroaching, a low lifetime band at the very top, and dislocation cascades in the upper two-thirds of the slice.

The low lifetime band at the top of the ingot is due to impurity segregation during the directional solidification of the ingot. During ingot cooling, impurities can diffuse back into the bulk of the ingot. This phenomenon is also observed in mc-Si cast silicon and CZ silicon. The low lifetime band at the side of the ingot is caused by impurities that have diffused in from the crucible walls, as previously described for the mc-Si silicon sample. The low lifetime band at the base of the Mono<sup>2</sup>™ slice is 5 cm wide, which is double the width of the low lifetime band in the cast mc-Si slice discussed in Chapter 1. Both ingots are cast in the same type of crucible and have almost identical casting times so similar amounts of crucible originating impurities are expected to be in both ingots. The contribution of crystal structure to the low lifetime band needs to be investigated.

Dislocation cascades seem to originate in the upper two-thirds of the ingot and shown in Fig. 1. The density of these cascades increases with elevation by branching visible to the naked eye. We would like to determine the origin of the cascades and understanding the nature of their branching in hopes that they could be eliminated in future crystal growth.

#### *Defect Transitions in the Low Lifetime Region*

Samples near the base of the slice were polished and Secco etched for varying durations and examined using Nomarski microscopy in order to gain understanding of the defects present in the crystal. The lifetime map shown in Fig. 1 shows the seed crystal near

the base of the ingot as curved orange triangle in the wide red band. There is a thin red line indicating very low minority carrier lifetime beneath the seed which corresponds to the structure observed in Fig. 2A. A possible cause of this structure is that liquid silicon seeps beneath the seed during melting and solidifies during cooling forming a thin layer of silicon. This explanation is supported by the fact that this feature is not present at the small region between the seed and the crucible sidewall visible in the lower left of the lifetime map shown in Fig 1. The large voids visible in Fig. 2A are possibly due to gas trapped beneath the seed as the melted silicon fills the small space beneath. The low lifetime in this thin layer can be explained by two causes. First, significant impurity segregation during solidification would not be possible for this thin layer since the seed above remains solid. Thus, impurities dissolved into the liquid from the crucible during melting will be present. Secondly, this layer is directly in contact with the crucible so impurities originating there will be found here at their highest concentration due to solid state diffusion. Since both ingots have solid state diffusion from the crucible being directly in contact with the ingot base, we would expect to see iron and oxygen in concentration levels similar to those observed in the mc-Si sample at the base as described in Chapter 1.

At the interface between the seed crystal and the grown crystal, a visible transition in crystal defects occurs as shown in Fig. 2B. The relatively low density of defects in the seed transitions to a higher density of dislocation pits in the grown Mono<sup>2</sup>™ crystal. Closer examination of these pits reveals that many come in associated pairs lining up on (100) planes (vertical and horizontal). This suggests these pits correspond to dislocation loops. These defects are present throughout the crystal in the low lifetime band.

At the transition from low to high lifetime approximately 5 cm from the base of the ingot another transition in the defect type occurs. Shown in Fig. 2C and D are Nomarski images from a sample Secco etched for 30 seconds. Figure 2C shows the region where the lifetime transitions from low to high, represented by the thin yellow band in the MW-PCD map. This region has a dramatically reduced density of defects compared to that shown at the top of Fig. 2B and throughout the low lifetime band. Just above this region, a transition to dense saucer pits occurs as shown in Fig. 2D. Attempts to image these pits with the SEM were unsuccessful as they do not exhibit significant contrast with the bulk silicon. Since their size is smaller they do not grow with extended etch times as they would for dislocation pits. It is possible that these saucer pits are small oxygen precipitates related to vacancy clusters or other vacancy related defects.

Dislocation loops like those present in the low lifetime region are caused by the agglomeration of silicon self-interstitials. The dramatic shift to vacancy related defects suggests a phenomenon typically associated with CZ crystal growth. During the growth of a silicon crystal from the liquid phase, two parameters determine the type of point defects that are incorporated into the crystal: the growth velocity,  $V$ , and the thermal gradient,  $G_0$ , across the solid-liquid interface. The ratio of  $V$  to  $G_0$  determines whether the growing crystal will be rich in vacancies or interstitials. At sufficiently high  $V$  or low  $G_0$ , the crystal will be rich in vacancies; at low  $V$  or high  $G_0$ , the crystal will be rich in interstitials. Interstitials can agglomerate to form dislocation loops in the crystal. Vacancies can form vacancy clusters. Both of these larger scale defects can interact with impurities present within the crystal.

(Voronkov 1982). These etching results in the low lifetime region show that point defect incorporation can be controlled through manipulation of the  $V/G_0$  ratio during casting of a Mono<sup>2</sup>™ ingot. This degree of control of crystal quality is not possible in mc-Si cast silicon because of the interfering influences of grain boundaries and high density networks of dislocations.

### *Chemical Impurities*

In the examination of the mc-Si silicon slice in Chapter 1, iron was found to be the primary contaminant whose distribution correlated with minority carrier lifetime. This contamination enters the ingot from the fused silica crucible. Mono<sup>2</sup>™ ingots are cast in the same crucibles as traditionally cast mc-Si ingots with similar casting times so Fe and other metallic impurities can be expected to be present. DLTS confirms this as shown in Fig. 3 with the FeB complex peak appearing at 52K. A second small minority carrier trap peak is visible in Figure 3 near 140K. The peak is broad suggesting extended defects, but its position is not reproducible from diode to diode so it is neglected in further discussion. No other metallic impurities are observed by DLTS indicating that they are either precipitated or found in concentrations below our detection level. A concentration profile of FeB with elevation is shown in Fig. 4. This data was collected from the region of the slice nearest the center of the ingot to reduce any contributions from the sidewall of the crucible. The maximum FeB concentration is  $2.2 \times 10^{13} \text{ cm}^{-3}$ , which is high enough to limit the minority carrier lifetime to a maximum value of 1  $\mu\text{s}$  (Istratov et al., 2000). The FeB concentration drops below the detection limit of  $5 \times 10^{11} \text{ cm}^{-3}$  at 5.2 cm elevation, which is where the low to

high lifetime transition occurs. We can therefore confirm that Fe contamination is the primary cause of the low lifetime band at the base of the Mono<sup>2</sup>™ ingot as it was in the mc-Si sample. The profile has an unexpected shape in that the FeB concentration is highest near the middle of the low lifetime band and not at the very base of the ingot, i.e., near the crucible that is the source. Interstitial iron in silicon has been shown to interact with vacancies to form stable and electrically inactive substitutional iron in p-type material (Estreicher et al, 2008). This is a possible explanation for the shape of the FeB concentration distribution. When the silicon interstitial concentration is high, the vacancy concentration is necessarily low since the two point defects annihilate each other. Thus, interstitial iron and iron complexed with substitutional boron would be expected to have higher concentrations where the silicon interstitial concentration is highest. The FeB concentration is low in the bottom 1 cm of the ingot which corresponds to the seed crystal. This seed crystal is initially CZ and would have lower self-interstitial levels than the crystal immediately above, which would mean higher vacancy levels. Thus the lower dissolved Fe concentration levels at the base of the ingot can be described by the point defect levels.

FT-IR was performed on the Mono<sup>2</sup>™ slice to determine the concentration profiles of interstitial oxygen and substitutional carbon and to see if they varied with defect type as the FeB concentration did. Both elements were detected by FT-IR as shown by the absorbance spectra in Fig. 5. During examination of the mc-Si slice in Chapter 1, oxygen and carbon concentration profiles were not found to correlate with minority carrier lifetime. As seen in Fig. 6, the same holds true in the Mono<sup>2</sup>™ ingot. Interstitial oxygen concentration smoothly decreases from a value of  $6.6 \times 10^{17} \text{ cm}^{-3}$  near the ingot base to  $6.0 \times 10^{16} \text{ cm}^{-3}$  at an elevation

of 20 cm. Correlation of the oxygen concentration to etching results is present only near the ingot base. The oxygen concentration profile is relatively flat in the bottom 1 cm of the ingot, which corresponds to the seed crystal. Above this elevation, the oxygen concentration gradually drops. Beyond this seed crystal, interstitial oxygen does not show a strong sensitivity to the defect type as the interstitial oxygen concentration profile does not have a dramatic shift to correspond with the change in defect type observed near 5 cm elevation. The substitutional carbon concentration is within the range of  $4.3 \times 10^{17} \text{ cm}^{-3}$  to  $9.9 \times 10^{17} \text{ cm}^{-3}$ . Its variation is more erratic than the oxygen concentration profile as visible in Fig. 6, which is likely due to difficulty in correctly subtracting the silicon phonon signal present very close to the substitutional carbon peak in the FT-IR absorbance spectrum. This can result in small errors in measurement that would make it difficult to resolve slight changes in concentration with elevation. Variations in this region could also be due to precipitation. The solubility limit of substitutional carbon is  $6 \times 10^{17} \text{ cm}^{-3}$  so the base of the ingot is supersaturated. We can still see that the carbon concentration profile is relatively flat with only a slight general decrease in concentration with increasing elevation. This trend matches the data collected for the mc-Si ingot.

#### *Dislocation cascades*

Samples were examined from the lowest elevation where dislocation cascades can first be observed in the MW-PCD lifetime map and from a region of dense cascades. These samples were polished and Secco etched for 3 minutes. Shown in Fig. 7A is a Nomarski image of precipitates causing nucleation of dislocations. These dislocations form in lines that

extend as the solid/liquid growth interface propagates. Such a “line” of dislocations is a small angle grain boundary. The right side of Fig. 7B shows the dislocation lines from Fig. 7A merging onto another line that crosses their path. After such a merging, the density of the dislocations in the resulting line is typically higher than those in its preceding lines. This means the angular misalignment in the small angle grain boundaries becomes larger after a merger. Figure 7C shows two more severe lines merging. Notice how these lines are curved suggesting that the propagation of these dislocation lines does not appear to have a preference for any specific crystallographic directions. Dislocation lines never terminate in bulk crystal and instead either merge with other lines or terminate at another defect. Figure 7D shows an example of line termination with a dislocation line terminating at a twin. If such a termination does not occur, these lines will eventually merge into a dislocation “cascade”, which are the diagonal features visible in the upper two-thirds of MW-PCD lifetime scan in Figure 1. These cascades are regions of very high dislocation density and high recombination activity as seen in the MW-PCD map. Although these cascades appear to lie on the same diagonal plane, the conclusion that these defects preferentially line up should not be made. The apparent direction of the cascades is due to the curvature of the growth interface. On the opposite side of the ingot, the cascades fan in the opposite direction and in the middle of the ingot they are vertical. The directionality of the cascades is only significant in that it indicates the shape of the growth interface assuming that the cascades propagate nearly perpendicular to the interface.

The density of dislocation cascades increases greatly with increasing elevation in the ingot. This suggests either increased formation of the cascades or branching of the cascades

resulting in multiplication. It would be expected that formation of new cascades via merging of lines is less of a contributing factor to the increase in cascade density as the density rises since lines would merge with pre-existing cascades instead of forming new ones. Thus we would expect that branching is the chief cause of the density increase. This is what is observed at higher elevations. Shown in Fig. 9 are examples of dislocation cascade branching. In these images, the growth direction is from bottom to top. This branching occurs in two seemingly different modes: acute angle and right angle branching. In an acute branching event, as shown in Fig. 8A and 8B, a cascade splits into two separate ones at a slight angle. In a right angle branch, the cascade seems to split into two separate cascades growing in opposite directions. Such a branching is shown in Fig. 8C and 8D. After a short distance of propagating in opposite directions, the two new cascades then proceed in the direction of crystal growth.

Shown in Fig. 9 is an SEM image of a right angle branching event. This sample has been Secco etched for three minutes and each pit visible in the image corresponds to a dislocation. The growth direction in this image is left to right. Notice that in the parent cascade at the left there appear to be two “canyons” running side by side. These canyons split into the two daughter cascades. In between the two daughter cascades directly beyond the split are some larger formations that are possible precipitates. Oxygen was detected by EDS at these features. Another feature of interest is the apparently “dark” dislocation pits. The other pits are “light” around their rims because of charging in the SEM. EDS only detects silicon at light pits, but Al, Ca, O, and C are detected at darkened pits with oxygen and carbon being the most consistent elements observed from pit to pit. When a similar

analysis was attempted on acute angle branches, no chemical species other than silicon were identified by EDS. This suggests that these two branching phenomenon as viewed in this plane are different and that contamination may play a role in causing right angle branching.

It is possible that both types of branching are the same phenomenon seen from different viewpoints. An acute angle branching event could be a right angle event where the propagation in opposite directions is extremely short. These cascades are grain boundaries that are two-dimensional surfaces present within a three-dimensional crystal and we only view them in the plane in which the crystal has been cut. Shown in Fig. 10 is an image of how dislocation cascades appear in a wafer cut parallel to the base of the ingot illustrating how these features extend in three dimensions. Thus another possibility is that an acute angle branching is a right angle branching observed outside of the plane in which the actual split occurs. The effects of dislocation cascades in this plane of view can be seen as forming small angle grain boundaries with very high dislocation density. The dislocations are frozen in place in the crystal during ingot cooling and cannot migrate and interact to form an equilibrium structure such as a more ideal small angle grain boundary with lower dislocation density.

#### *Comparison of Multi- and Monocrystalline Casting*

The mc-Si and Mono<sup>2</sup><sup>TM</sup> ingots are cast in almost similar fashion. Both ingots are cast in the same furnaces, use the same type of crucible, and have similar casting times. Both are solidified directionally from bottom to top. The primary difference between the two casting methods is the seed crystal which results in single crystal growth of the Mono<sup>2</sup><sup>TM</sup>

ingot. These similarities allow for direct comparison between the two casting methods. The difference in crystal defects is clear at first glance. The mc-Si sample is filled with grain boundaries of all types and there is variation among grains between high and low dislocation density. The Mono<sup>2</sup>™ sample has small angle grain boundaries surrounded by a high density of dislocations that we have termed “dislocation cascades”. At lower elevations, the defect type and density are controlled by V/G<sub>0</sub> growth conditions as with CZ silicon. The general difference between the two casting methods relative to defects is that Mono<sup>2</sup>™ casting allows greater control during manufacturing of the defect type and density. In mc-Si silicon, some grains experience high stress during casting and form dislocations as a result which would disrupt any engineered defect distribution controlled by V/G<sub>0</sub> growth conditions.

Iron was found to be the primary lifetime reducing impurity in both ingots, but its distribution was significantly different between them. In Chapter 1, Fig. 8, the iron concentration in the mc-Si ingot is shown to decrease with elevation from an average value of  $4.7 \times 10^{12} \text{ cm}^{-3}$  over the bottom 1.5 cm of the ingot to below the detection level of about  $1.5 \times 10^{12} \text{ cm}^{-3}$  at an elevation of 2.25 cm. The profile for the mc-Si sample is not smooth due to grain to grain variation in iron concentration. The iron concentration in the Mono<sup>2</sup>™ ingot is  $1.3 \times 10^{12} \text{ cm}^{-3}$  for the bottom 1 cm of the ingot corresponding to the seed crystal. Above this elevation, the iron concentration rises to a maximum value of  $2.2 \times 10^{13} \text{ cm}^{-3}$  at an elevation of 2.9 cm before dropping below the detection limit of  $5 \times 10^{11} \text{ cm}^{-3}$  at 5.2 cm above the ingot base. The shape of the iron distribution in the Mono<sup>2</sup>™ ingot appears to be related to the structural defect type present at different elevations. The detection limit is higher for

the mc-Si ingot because of a higher level of noise in the capacitance transient, perhaps caused by leakage in the diodes due to a high density of dislocations beneath them. The iron concentration is more than double at its maximum in the Mono<sup>2</sup>™ sample and the detectable iron extends to double the elevation than in the mc-Si sample.

Similar trends in concentration level are present in the light element impurities as well. Shown in Fig. 11 is a plot of the FT-IR determined interstitial oxygen levels with elevation near the center of both ingots. FT-IR concentration profiling was performed in the Mono<sup>2</sup>™ sample from the base of the ingot towards the top, but for the mc-Si sample from the side of the ingot towards the center at three different elevations. For this reason, there are only three data points available from the mc-Si sample for comparison between the two casting methods. These points are an average of the interstitial oxygen concentrations for the flat portion of the profiles shown in Chapter 1, Figs. 4 and 6. The oxygen distribution in both casting types has the same general shape of a decrease with increasing elevation. Both ingots have nearly identical oxygen concentration levels between  $1\text{-}1.5 \times 10^{17} \text{ cm}^{-3}$  above 10 cm elevation. The difference is in the magnitude of the concentrations near the ingot base. The mc-Si interstitial oxygen is about  $3 \times 10^{17} \text{ cm}^{-3}$  near the ingot base while the Mono<sup>2</sup>™ ingot has  $6.5 \times 10^{17} \text{ cm}^{-3}$  at its base. Substitutional carbon was observed to decrease with elevation in both ingots but as with interstitial oxygen, the Mono<sup>2</sup>™ ingot contains significantly more than the mc-Si ingot. The mc-Si ingot has an average substitutional carbon concentration of  $1.0 \times 10^{17} \text{ cm}^{-3}$  at the 7 cm elevation and  $5.4 \times 10^{16} \text{ cm}^{-3}$  at an elevation of 21 cm, while the Mono<sup>2</sup>™ ingot has an average concentration of  $8.2 \times 10^{17} \text{ cm}^{-3}$  near the ingot base and  $4.6 \times 10^{17} \text{ cm}^{-3}$  at an elevation of 19 cm. The carbon level in the in the entire Mono<sup>2</sup>™

sample is nearly an order of magnitude higher than in the mc-Si silicon at similar elevations. The solubility limit of carbon in silicon is near  $6 \cdot 10^{17} \text{ cm}^{-3}$  meaning that the Mono<sup>2</sup>™ silicon is supersaturated with carbon while the mc-Si ingot is not.

Interstitial oxygen is expected to be slightly higher as a result of the Mono<sup>2</sup>™ casting method due to oxygen contributions from the seed crystal. Integrating beneath the oxygen concentration vs. elevation plot gives the total number of oxygen atoms per square centimeter of the ingot base. Subtracting the difference of such an integral gives the total oxygen atom difference per square centimeter of ingot base. The difference for these two ingots is  $1.8 \cdot 10^{19}$  oxygen atoms per square cm of ingot base. From the small orange wedge at the base visible in the lifetime map shown in Figure 1, we can estimate the thickness of the seed crystal as 1 cm thick. A CZ seed crystal with  $1 \cdot 10^{18} \text{ cm}^{-3}$  oxygen with 1 cm thickness would only contribute  $1 \cdot 10^{18}$  oxygen atoms per square centimeter of base. This contribution is only about 5% of the observed oxygen difference so the seed crystal is clearly not the source of most of the additional oxygen in the Mono<sup>2</sup>™ ingot. There are no other apparent sources of additional chemical impurities for the Mono<sup>2</sup>™ silicon since both ingots are cast in such similar manners.

A possible explanation for the elevated dissolved impurity levels in the Mono<sup>2</sup>™ ingot is that the mc-Si ingot contains similar total amounts of impurities, but more is unavailable for measurement in mc-Si silicon. Iron can only be detected by DLTS if it is electrically active. Oxygen is detected by FT-IR if it is on an interstitial site in silicon or if forms silicon dioxide precipitates of specific shapes. Carbon can only be detected by FT-IR if it lies on a silicon lattice site. The elevated density of dislocations and grain boundaries in

the mc-Si sample can serve as sites for precipitation and gettering. Slight differences in the introduction of impurities should be considered as well. Considering only total iron concentration and ignoring effects of defects and precipitation, the low lifetime band at the base in a Mono<sup>2</sup>™ ingot can be expected to be slightly wider by roughly the thickness of the seed than in a mc-Si ingot because the Fe gets a “head start” on solid state diffusion since the seed remains solid during feedstock melting. In mc-Si casting, the entire base of the crucible provides a source of impurities to the liquid silicon while in the Mono<sup>2</sup>™ process the bulk of the liquid is shielded from this surface by the seed. Iron and other impurities originating at the crucible base still enter the liquid silicon above, but the seed reduces the speed at which diffusion can occur since solid state diffusion is slower than diffusion through the liquid phase. Even though the low lifetime band is expected to be slightly wider in the Mono<sup>2</sup>™ ingot, the total impurity concentration in this ingot should be lower than in a mc-Si ingot because of the seed’s role as a diffusion barrier.

## **Conclusion**

The data in this chapter has revealed much about the Mono<sup>2</sup>™ ingot and its growth process. Defect delineation etching has shown that the Mono<sup>2</sup>™ crystal growth shares control of point defect incorporation with CZ silicon, an advantage not present in mc-Si cast growth. The impurities present in mc-Si silicon are also present in Mono<sup>2</sup>™, but the distributions of these impurities differ greatly. The distributions in Mono<sup>2</sup>™ ingots are sensitive to the point defect distributions. The magnitudes of the dissolved impurity concentrations are 2-10 times higher than in mc-Si silicon even though the total

concentration of impurities in Mono<sup>2</sup>™ ingots should be less. This is because mc-Si silicon has grain boundaries and higher densities of dislocations that serve as gettering sites. Impurities also affect the crystal quality. Silicon carbide precipitates have been shown to cause the nucleation of small angle grain boundaries. These boundaries, also termed “dislocation lines”, merge to form “dislocation cascades” which are small angle grain boundaries with high density of surrounding dislocations. These cascades multiply with increasing elevation due to two possibly different branching processes. One of these branching processes, right-angle branching, appears to occur in the vicinity of impurity precipitation. Crystal quality and impurity distributions are not independent parameters in the Mono<sup>2</sup>™ growth process. Progress towards perfecting Mono<sup>2</sup>™ silicon for solar substrates will require refined control of impurity introduction and growth parameters.

## Figures

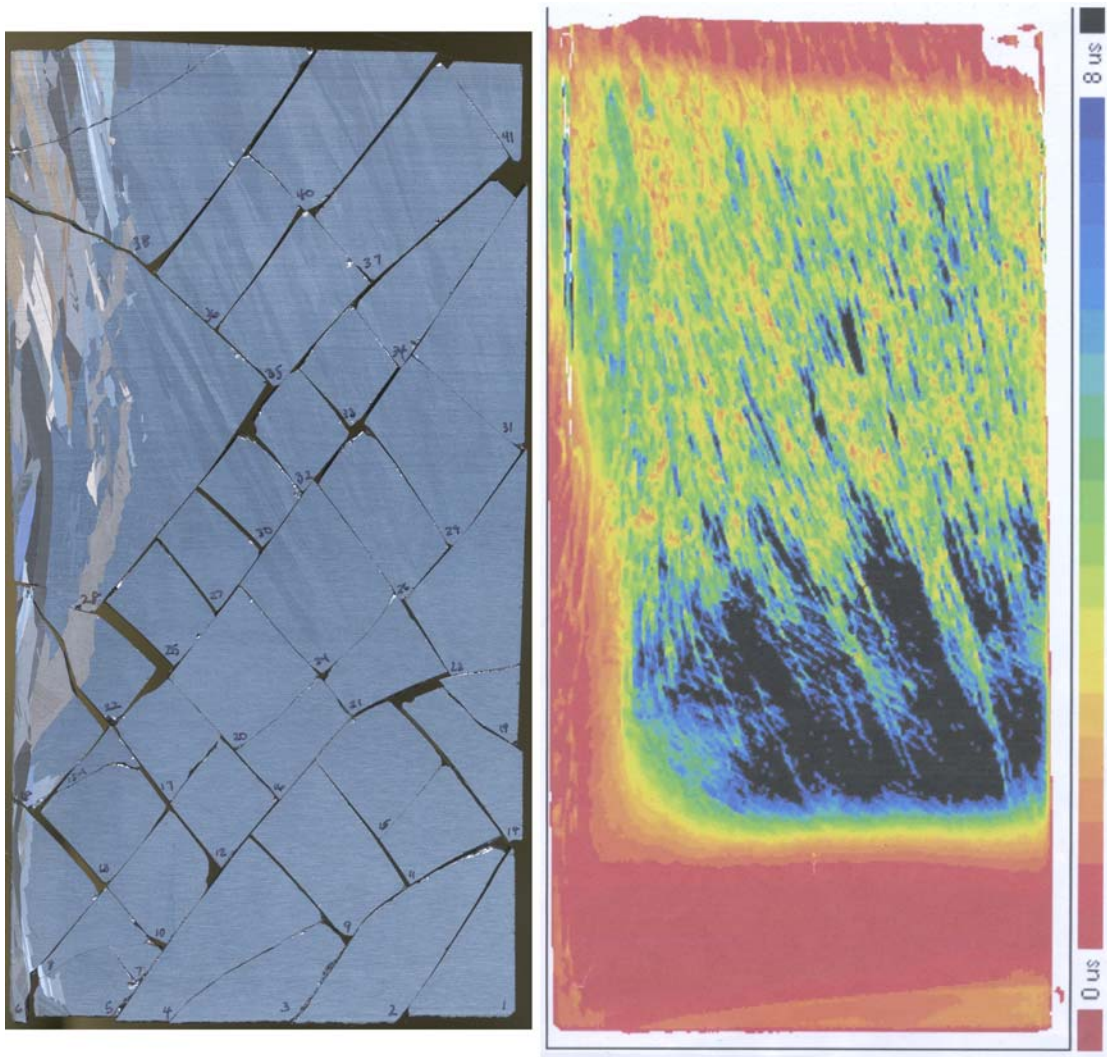


**Figure 1: Scan and MW-PCD lifetime map of monocrystalline sample. At left, scan of the reassembled pieces of the Mono<sup>2</sup> slice. At right, MW-PCD minority carrier lifetime scan of the slice before cleaving.**

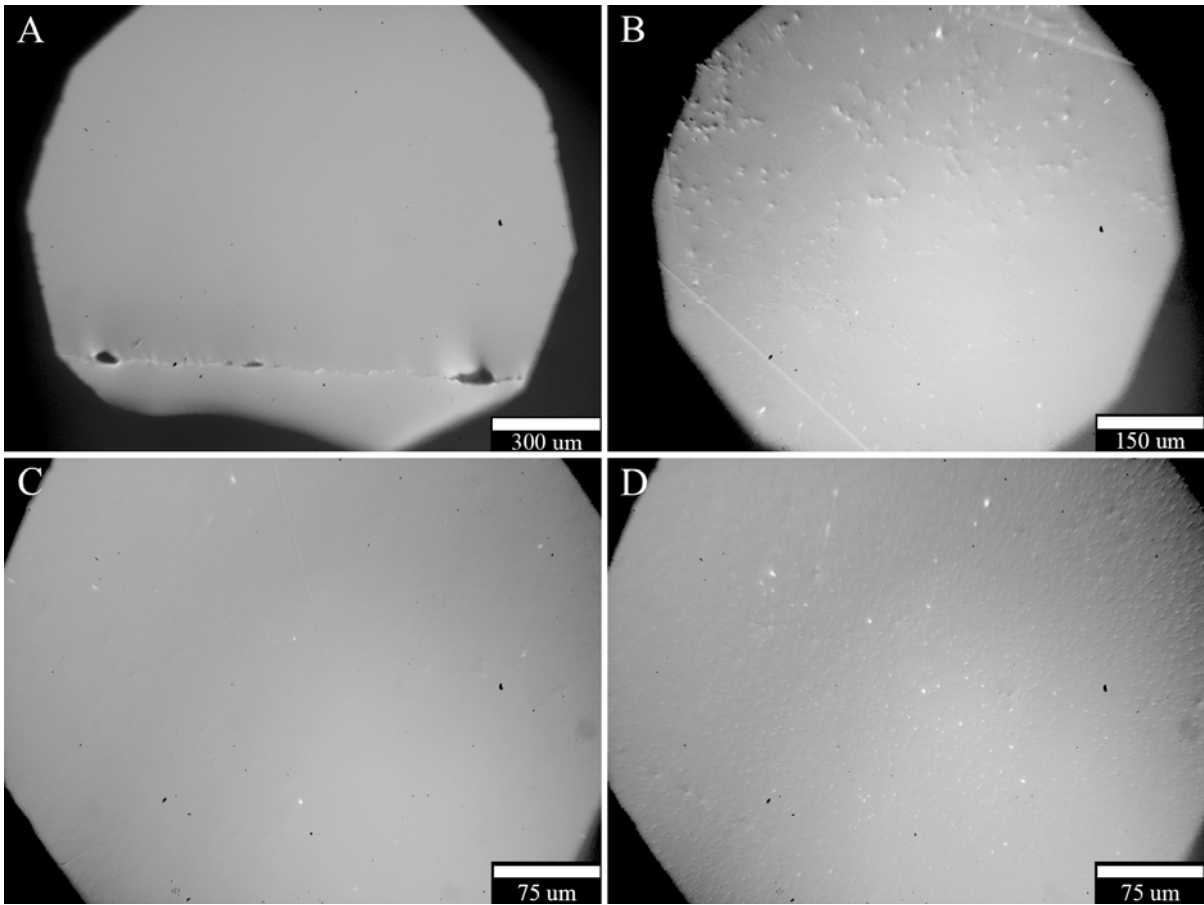


**Figure 2: Composite of Nomarski images showing transitions in etch pit defect type with elevation in Mono<sup>2</sup> ingot. Image A shows the boundary beneath the seed caused by liquid silicon seeping beneath the seed during feedstock melting. Image B shows the transition from the seed crystal (bottom) to the grown monocrystal which contains dislocation loops. Image C shows the region of transition from low to high lifetime. Very few defects are present at this transition. Image D shows very small pit features in a high density. This image is from a region of high lifetime and it is possible that these pits are caused by oxygen precipitation or vacancy clusters.**

### 28.8 mm Elevation DLTS Spectrum

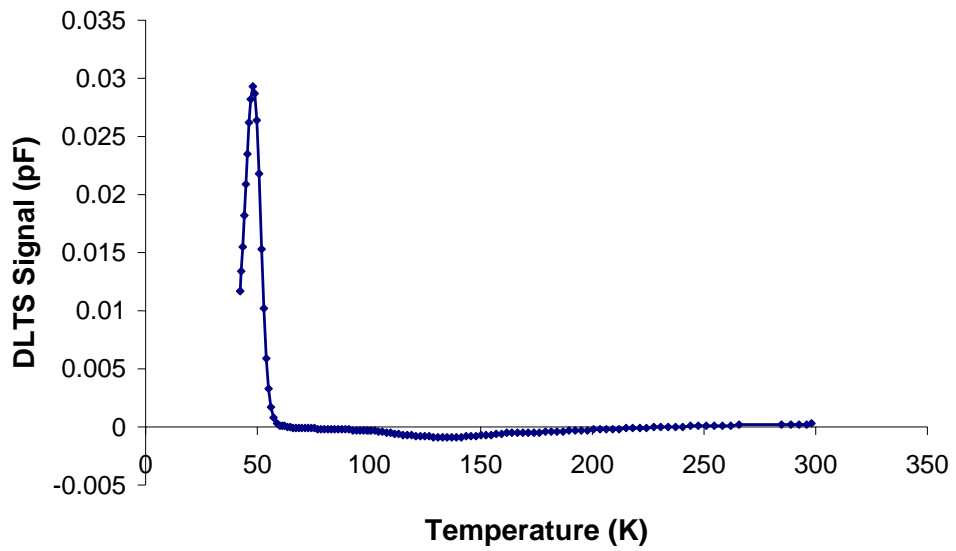


Figure 3: Sample DLTS Spectrum from 28.8 mm elevation. The Fe-B peak is visible at 52K.

### [FeB] with elevation in Mono2

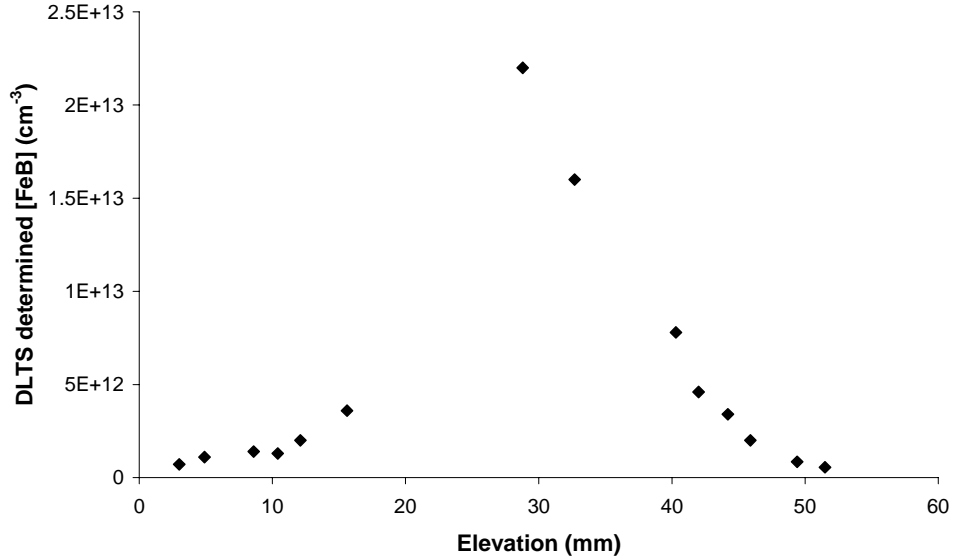
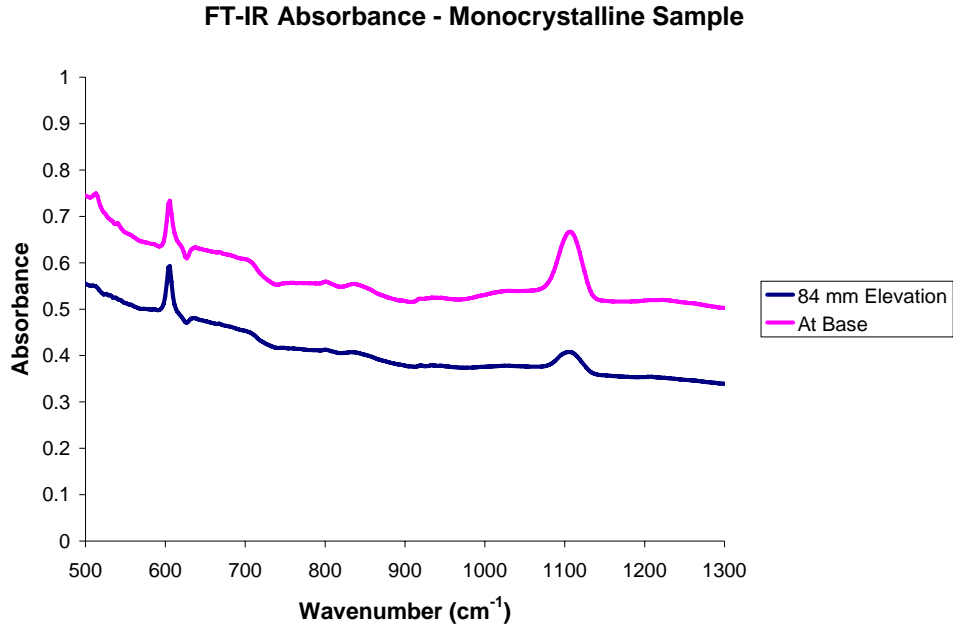
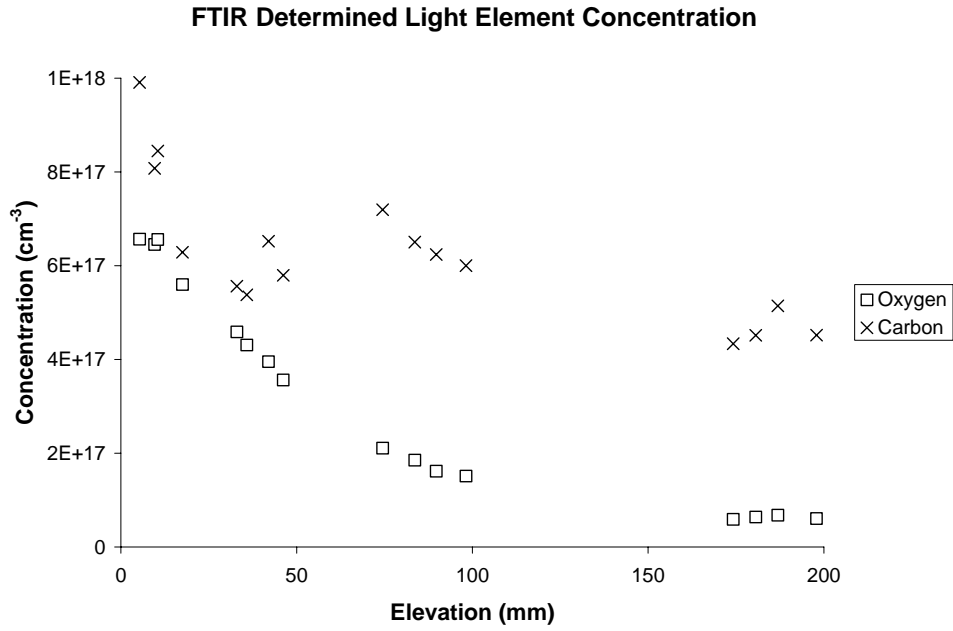


Figure 4: DLTS determined Fe-B concentration with elevation in the Mono<sup>2</sup> ingot.



**Figure 5:** FT-IR absorbance spectra for monocrystalline sample. The interstitial oxygen peak at  $1107\text{ cm}^{-1}$  is considerably larger near the ingot base than at 84 mm elevation.



**Figure 6:** FT-IR determined light element impurity concentration profiles in a monocrystalline ingot.

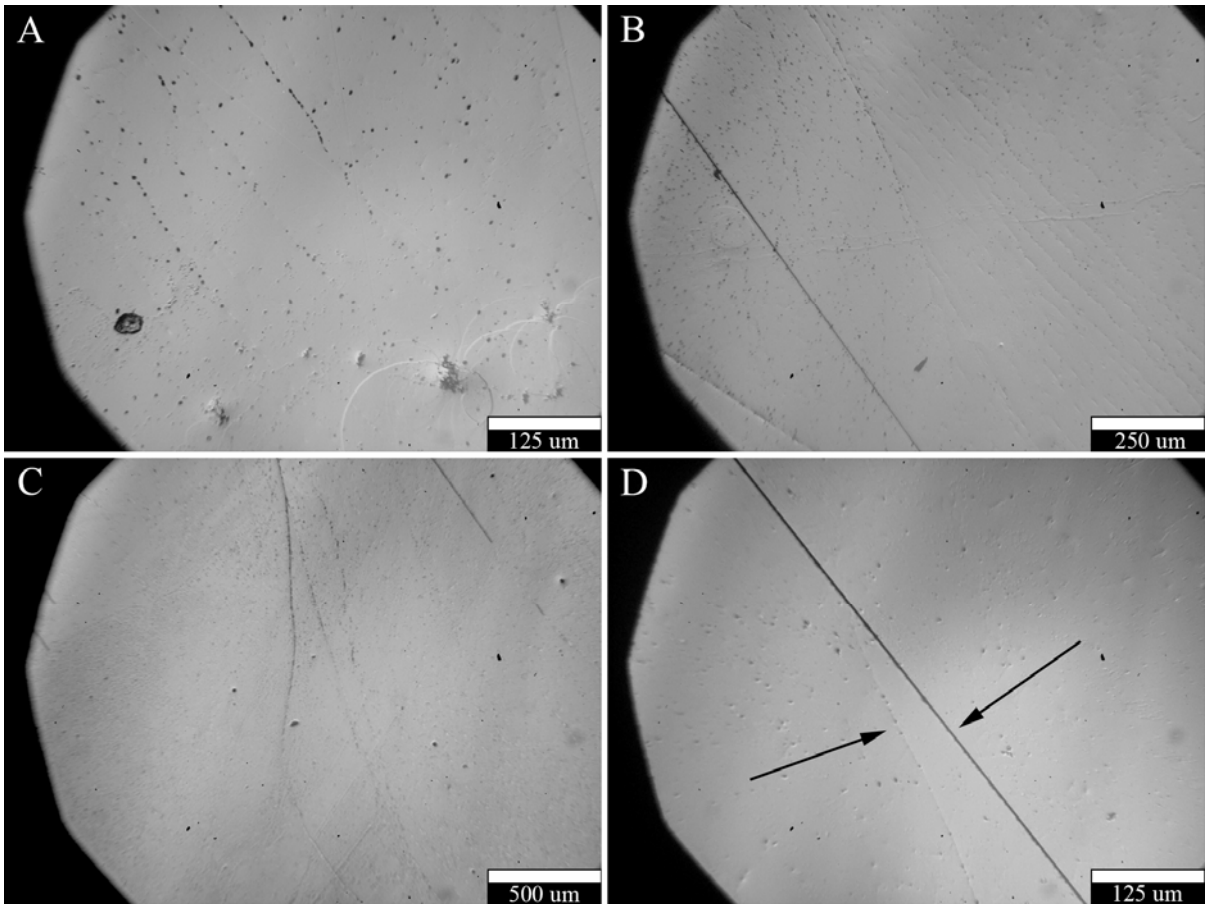


**Figure 7: Nomarski images showing behavior of dislocation lines. Image A shows precipitates causing dislocation lines that propagate with the growth direction. Image B shows the lines from Image A visible in the right half of the image merging with other lines. Image C shows a merging of two dislocation lines with higher dislocation density. Image D shows a dislocation line (left arrow) terminating at a twin (right arrow).**

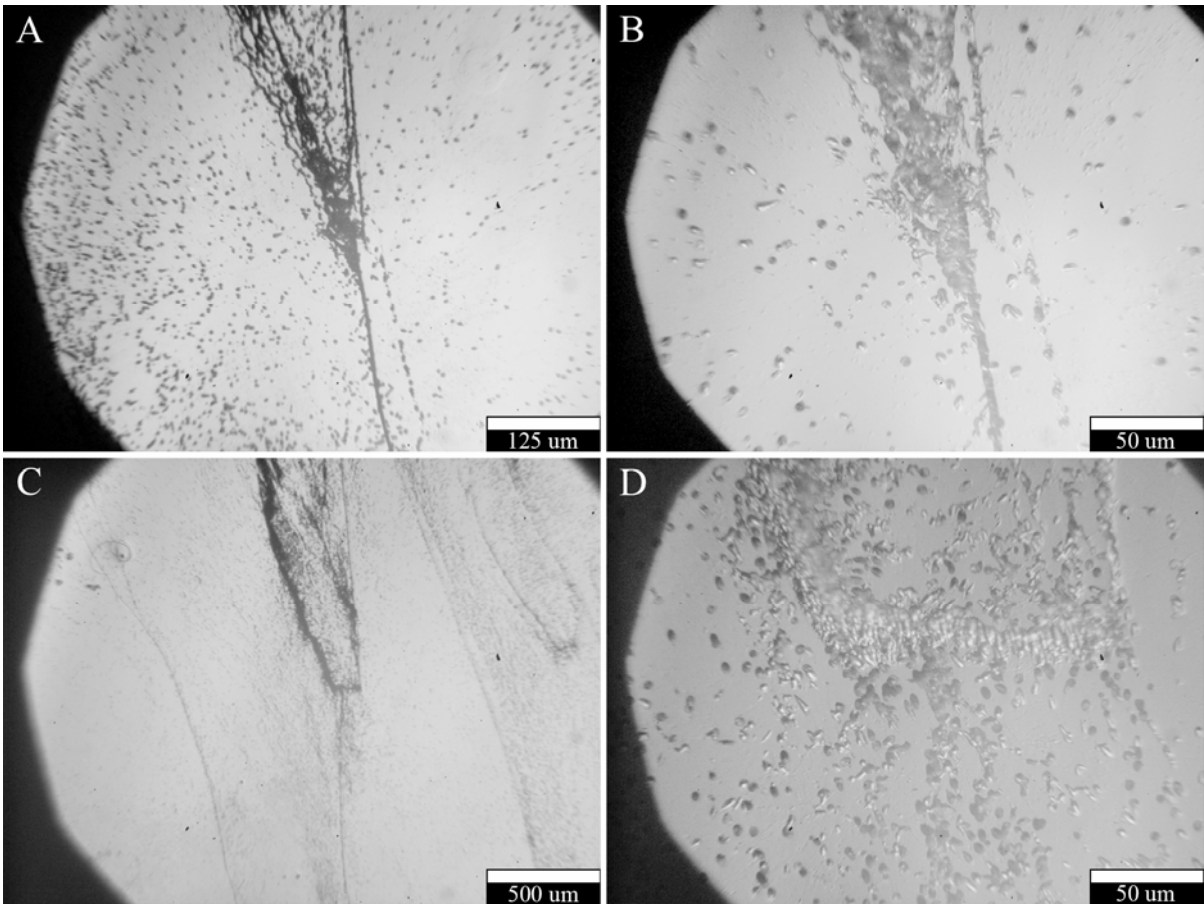


**Figure 8: Nomarski images illustrating dislocation cascade branching. Image A shows an acute angle branching. Image B is a higher magnification image of the same branching. Image C shows a right angle branching event. Image D is a higher magnification image of the branching in Image C.**

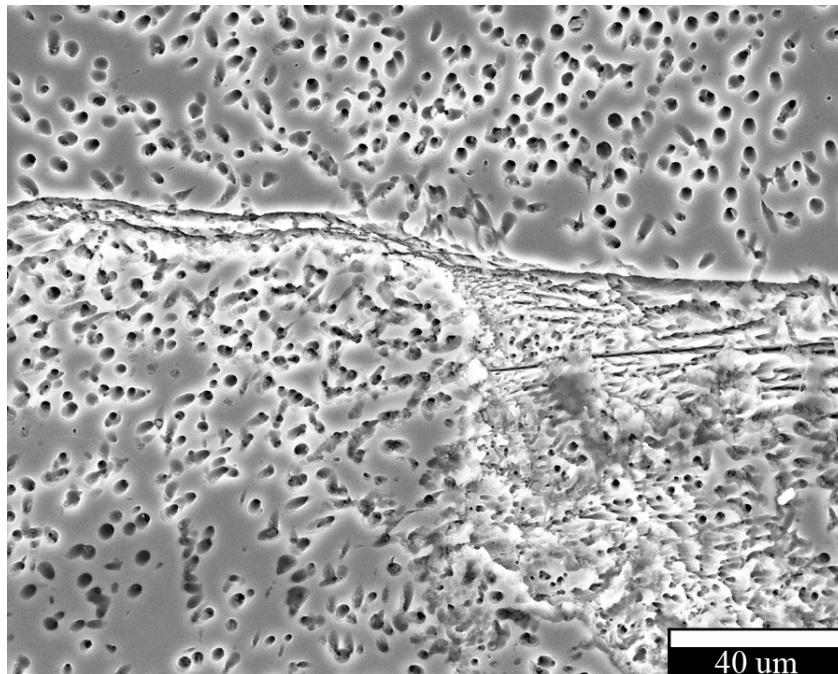


**Figure 9:** Secondary electron SEM image showing a right angle dislocation cascade branching. Crystal growth direction is from left to right. Oxygen and carbon were detected by EDS between the two daughter cascades.

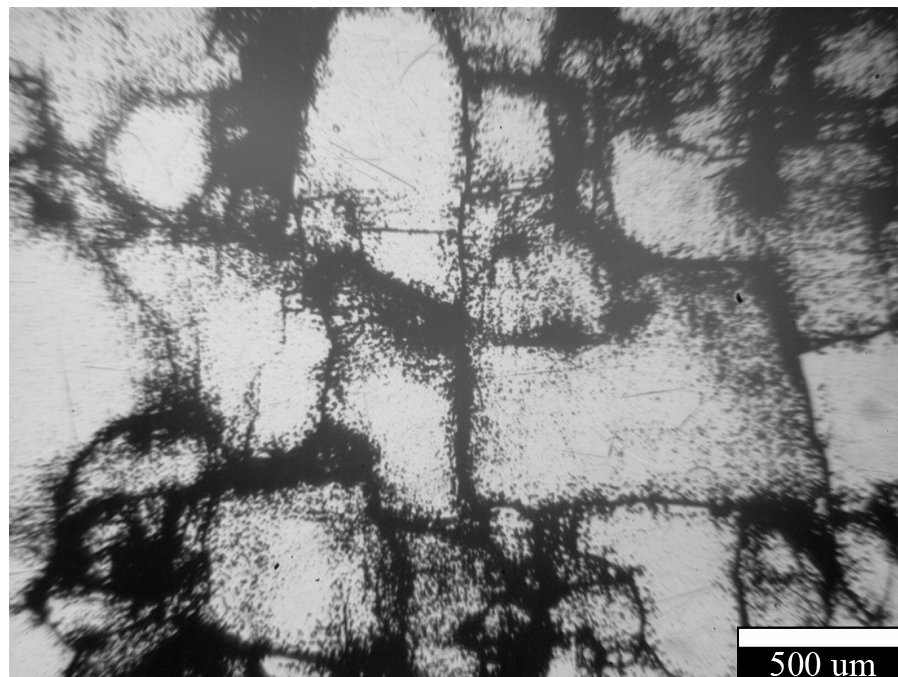


**Figure 10:** Dislocation cascades viewed from a plane parallel to the ingot base. The image is a Nomarski image of a sample Secco etched for 3 minutes. The cascades cause the formation of small angle grain boundaries with high surrounding dislocation density.

### FT-IR Determined Interstitial Oxygen

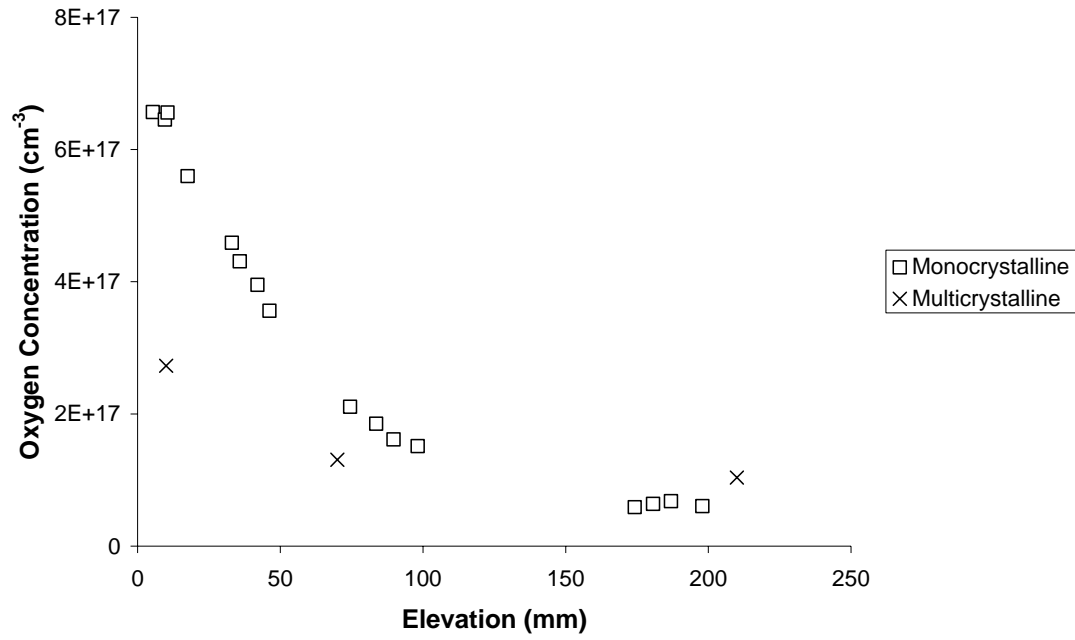


**Figure 11: Comparison of interstitial oxygen levels with elevation in monocrystalline and multicrystalline ingots. The monocrystalline ingot is shown to have nearly double the oxygen concentration of the multicrystalline ingot at elevations below 10 cm.**

## REFERENCES

**Stoddard, N. (2007).** *U.S. Patent Number No. 084934*, Washington, DC: U.S. Patent and Trademark Office.

**Stoddard, N., Wu, B., Witting, I., Wagener, M., Park, Y., Rozgonyi, G., & Clark, R. (2008).** Casting single crystal silicon: Novel defect profiles from BP Solar's Mono<sup>2</sup>™ Wafers. *Solid State Phenomena*, 131, 1-8.

**Voronkov, V. V. (1982).** The mechanism of swirl defects formation in silicon. *Journal of Crystal Growth*, 59, 625-643.

**Secco D'Aragona, F. (1972).** Dislocation etch for (100) planes in silicon. *Journal of the Electrochemical Society*, 119(7), 948-951.

**ASTM International (2002).** F1188 – Standard test method for interstitial atomic oxygen content of silicon by infrared absorption with short baseline. *ASTM Standards*

**ASTM International (2000).** F1391 – Standard test method for substitutional atomic carbon content of silicon by infrared absorption. *ASTM Standards*

**Istratov, A. A., Hieslmair, H., & Weber, E. R. (2000).** Iron contamination in silicon technology. *Applied Physics A*, 70, 489-534.

**Estreicher, S. K., Sanati, M., & Gonzalez Szwacki, N. (2008).** Fundamental interactions of Fe in silicon: First-principles theory. *Solid State Phenomena*, 131, 233-240.

## CLOSING REMARKS

In this thesis, I have discussed two different methods of casting silicon for solar substrates. Although both methods utilize the same furnaces and crucibles, the impurity and defect profiles in the ingots produced by each method are quite different. Monocrystalline cast silicon (Mono<sup>2</sup>™) was found to exhibit point defect incorporation that depended on growth parameters in the same way that Czochralski (CZ) silicon does. Multicrystalline cast silicon (mc-Si) does not exhibit such behavior because the grain boundaries act as interfering influences in point defect distributions and serve as gettering sites for impurities. Electrically active impurity distributions in Mono<sup>2</sup>™ were found to correlate with distributions of point defects. Due to the casting process, the levels of some impurities in this material are significantly higher than those in CZ silicon. Thus Mono<sup>2</sup>™ silicon provides a unique system for the study of impurity interaction with point defects. While it has laid the foundation for deeper understanding of the Mono<sup>2</sup>™ growth process, the research presented in this thesis has only identified large scale trends. As I continue at NC State University towards my doctorate degree, my research will focus on the control of point defect incorporation and impurity interaction within Mono<sup>2</sup>™ silicon. Future work will focus on understanding what forms point defects exist as within this material. For example, we will attempt to answer whether vacancies exist as point defects or as agglomerations and what concentration they are present at. This work will be accomplished using techniques such as transmission electron microscopy.